Finite-wavelength scattering of incident vorticity and acoustic waves at a shrouded-jet exit

ARNAB SAMANTA[1] AND JONATHAN B. FREUND[1,2]

[1]Department of Mechanical Science and Engineering, University of Illinois at Urbana–Champaign, Urbana, IL 61801, USA

[2]Department of Aerospace Engineering, University of Illinois at Urbana–Champaign, Urbana, IL 61801, USA

As the vortical disturbances of a shrouded jet pass the sharp edge of the shroud exit some of the energy is scattered into acoustic waves. Scattering into upstream-propagating acoustic modes is a potential mechanism for closing the resonance loop in the 'howling' resonances that have been observed in various shrouded jet configurations over the years. A model is developed for this interaction at the shroud exit. The jet is represented as a uniform flow separated by a cylindrical vortex sheet from a concentric co-flow within the cylindrical shroud. A second vortex sheet separates the co-flow from an ambient flow outside the shroud, downstream of its exit. The Wiener–Hopf technique is used to compute reflectivities at the shroud exit. For some conditions it appears that the reflection of finite-wavelength hydrodynamic vorticity modes on the vortex sheet defining the jet could be sufficient to reinforce the shroud acoustic modes to facilitate resonance. The analysis also gives the reflectivities for the shroud acoustic modes, which would also be important in establishing resonance conditions. Interestingly, it is also predicted that the shroud exit can be 'transparent' for ranges of Mach numbers, with no reflection into any upstream-propagating acoustic mode. This is phenomenologically consistent with observations that indicate a peculiar sensitivity of resonances of this kind to, say, jet Mach number.

1. Introduction

1.1. *Resonances in shrouded jets*

The potential for shrouded jets, or jets fitted with an ejector (see figure 1), to resonate making high-intensity discrete-frequency sound was first reported almost forty years ago by Bradshaw, Flintoff & Middleton (1968) and was called howling. Seemingly similar resonances have also been observed in full-scale turbojet engine test cells (see Jones & Lazalier 1992; Sebourn & Shope 2005; Massey *et al.* 1994). Here, intense tonal pressure fluctuations were observed in the shroud near its inflow end with the resonance frequency closely matching the first asymmetric acoustic modes expected in the shroud: the so-called $(m, n) = (1, 1)$ mode, where m and n correspond respectively to the azimuthal and radial wavenumbers.

How these resonances are sustained inside the shroud is not fully understood. It is expected that for high amplitudes the acoustic modes can excite the jet instability mode by perturbing the jet at the nozzle. Generally, jets are receptive to such
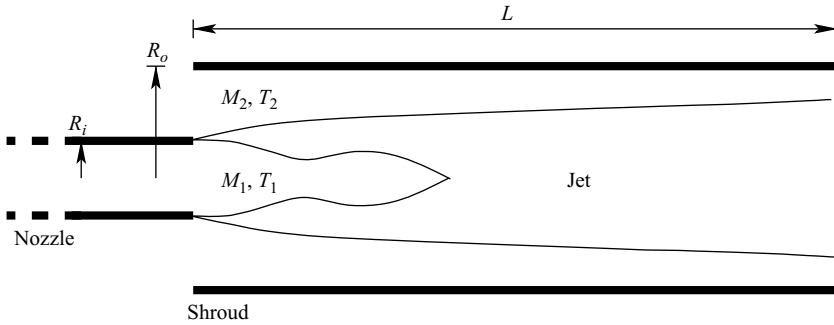
FIGURE 1. Schematic of a shrouded jet reported to howl.

excitations at the nozzle lip and the resulting instabilities should grow by extracting energy from the jet at their respective frequencies. It is uncertain, however, how these flow instabilities generate pressure fluctuations to reinforce the shroud acoustic modes and thereby close the feedback loop. There are several theories for this, including the one that depends upon jet shock cells, described by Tam, Ahuja & Jones (1994). But strong resonances have also been observed for subsonic jets. For example, Bradshaw *et al.* (1968) report subsonic confined jets that for ranges of Mach numbers resonate with tones 20 dB above the corresponding non-resonating spectrum of the jet. Consequently, they speculated that the instability (vorticity) waves supported by the inner shear layer interact with the nozzle shroud in a way that reflects waves with pressure fluctuations matching the frequencies of the shroud acoustic modes. This mechanism for closing the feedback loop was included by Howe (1987) in his analysis under the assumption that the shroud exit is effectively at a constant pressure. This is a long-wavelength assumption. In actual situations, however, the wavelength of the sound in the resonance modes is usually comparable to the shroud length, which in turn is comparable to its diameter (e.g. Jones & Lazalier 1992; Sebourn & Shope 2005). It is well known that for open-exit configurations, reflections of out-going acoustic waves are significantly reduced when these lengths are comparable (e.g. Levine & Schwinger 1948).

In this paper, we analyse the acoustic reflection of finite-wavelength vortical disturbances with the goal of illuminating the role of vortical flow disturbances in sustaining shroud resonances of the kind discussed. The model geometry we analyse is shown in figure 2. It consists of a semi-infinite cylindrical shroud with a co-flowing inner jet issuing out of it. The uniform inner, outer and ambient flows are separated by vortex sheets, with the outer vortex sheet originating at the shroud exit. The Wiener–Hopf method is used to calculate how vorticity waves on the inner shear layer scatter at the shroud exit into acoustic waves. Those reflected back upstream into the shroud have the potential to close the feedback loop. Although the main focus of this work remains the incident vorticity modes, the reflectivities of finite-wavelength outgoing acoustic modes are obtained with little extra effort. These are reported both for completeness and because their reflection is also important for any acoustically coupled resonance that might occur.

1.2. *Analysis as a Wiener–Hopf problem*

Acoustic wave reflection from a sharp-ended duct without mean flow was first solved by Levine & Schwinger (1948) using the Wiener–Hopf method (see Noble 1988). They obtained analytical expressions for sound waves radiated and reflected from the open

end of the duct. Mean flow was first included by Carrier (1956), whose analysis was consistent with taking Lorentz transformation of the no-flow case in a way that yields solutions both for flow into the duct, which makes the duct-lip singularity integrable, and for flow out of the duct, where the Kutta condition is automatically satisfied for this solution method. Later, Homicz & Lordi (1975) seem to have rediscovered this technique. However, for the exhaust case, a vortex sheet appears at the trailing edge, which needs to be included in the analysis. Mani (1973) derived a solution for the two-dimensional case with a velocity discontinuity that was extended by Savkar (1975) to a cylindrical geometry. However, none of these solutions included instability waves, since their correct mathematical treatment remained unclear, nor do they contain any proper treatment of the Kutta condition.

Morgan (1974) and Crighton & Leppington (1974) independently concluded that when a vortex sheet is shed from a semi-infinite plate the Kelvin–Helmholtz instability wave must couple to the acoustic field. They recognized that ignoring this wave yields a fundamentally incorrect field and developed procedures for its inclusion. The difficulty in identifying the correct Kutta condition formulation at the duct exit has been explained by Orszag & Crow (1970) and Crighton (1972a, b). The current accepted practice is to use the full Kutta condition (Crighton & Leppington 1974), which has experimental support (Bechert & Pfizenmaier 1975).

Munt (1977) was the first to combine all these related theoretical developments to construct a complete analytical solution for the transmitted waves for a subsonic jet issuing out of a semi-infinite cylindrical duct. His analysis placed no restriction on the velocities of the uniform subsonic jet or the co-flow, separated by a cylindrical vortex sheet, and also accounted for density and temperature jumps across the vortex sheet. Excellent agreement was obtained with the measurements of far-field directivity (Pinker & Bryce 1976) and reflection coefficients (see Munt 1990). The near-field features of Munt's results were confirmed by Howe (1979) using different analytical methods.

Using Munt's framework, the problem of a semi-infinite duct with an infinite centrebody in a uniform mean flow was first considered by Rienstra (1984). This was recently extended by Gabard & Astley (2006) to have different velocities inside and outside the duct with the consequence that instability waves had to be accounted for in the complete solution. Though the flow with a centrebody rather than a jet is, of course, significantly different from the present configuration, we use similar techniques here. Taylor, Crighton & Cargill (1993) analysed the same basic configuration as we do here (figure 2), but only for plane waves in the long-wavelength limit. Instead of solving the full Wiener–Hopf problem they solved two subproblems: first, sound transmission from a cylindrical nozzle into an infinite outer cylindrical duct; and second, sound transmission from a semi-infinite cylindrical duct containing a co-flow. These two problems were then matched by using plane-wave coupling. We use a similar two-part approach to generate the incident vorticity wave. These methods have also been applied to rotating flows (Heaton & Peake 2005). Uniform mean flow is, however, sufficient for studying the phenomena of present interest.

Recent works by Veitch & Peake (2007) and Demir & Rienstra (2007) have considered the far-field sound from the configuration of figure 1 by solving the full problem using a matrix Wiener–Hopf technique (details in Veitch & Peake 2008). These papers make an important advance in developing techniques to factor matrix Wiener–Hopf kernels. In the present work we focus entirely on near-field interactions, where our scalar approach seems more appropriate since it allows us to separately consider different incident wave solutions and explicitly compute their individual interactions
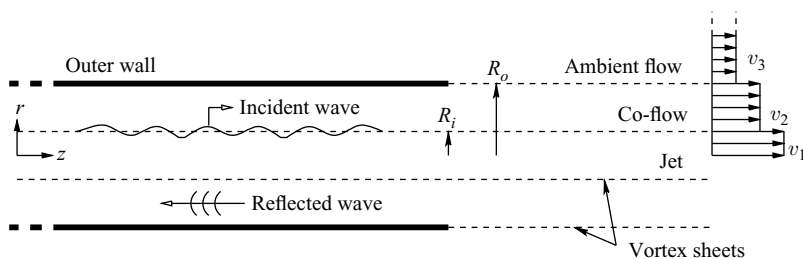
FIGURE 2. Schematic of the shroud with co-flow.

at the shroud exit. Of course, the full solution provided by matrix Wiener–Hopf techniques contains these interactions, but it would seem to require significantly more work to extract the individual interactions of interest. Even after solving the problem by the matrix approach, Veitch & Peake (2008) employ a scalar approach to identify how specific interactions contribute to the far-field sound. Obviously, interaction with the inner nozzle lip, not considered here, becomes important in determining the actual resonance conditions inside the shroud. We prefer to solve that particular problem by splitting the configuration of figure 1 into two subproblems, as done by Taylor *et al.* (1993) in the long-wavelength limit, which clarifies the physical picture better.

Extension to finite frequencies and vortical waves is essential for the kind of interaction that we consider. The behaviour of the vorticity wave passing the shroud edge in the short-wavelength limit is clear. Since the pressure disturbances associated with subsonic vortex sheet modes decay exponentially away from the sheet, for vanishingly short-wavelength there is no interaction between the vortex sheet modes and the shroud exit and thus no reflection. In the long-wavelength limit, such as the one considered by Taylor *et al.* (1993) for incident acoustic modes, the only reflected acoustic mode that the system can support is the plane wave, or more precisely a quasi-plane wave, since a true plane wave is impossible to define for multiple streams inside a duct. Our investigation of the observed asymmetric-mode resonances requires inclusion of modes that only propagate for finite frequencies. In this study, we also specifically focus on the scattering of the vorticity wave into acoustic modes, which has not been systematically studied before.

The organization of the paper is as follows. The governing differential equations and boundary conditions are described in §2. The Wiener–Hopf solution for a general incident wave is obtained in §3. Specific incident waves are defined in §4, and near-field visualizations for specific acoustic and vorticity incident modes are presented in §5. Reflectivity coefficients are formulated and computed in §6 for both acoustic and vorticity incident waves.

2. Formulation

The semi-infinite $(-\infty < z < 0)$ cylindrical shroud has radius R_o (see figure 2). Its walls are assumed to be rigid, impermeable, and of negligible thickness. The primary flow in the shroud is a jet of radius $R_i < R_o$ with uniform axial mean flow velocity v_1. The co-flow has uniform axial velocity v_2 for $R_i < r < R_o$. There is also an ambient flow external to the shroud $(r > R_o)$, which has a uniform axial velocity of v_3. Cylindrical vortex sheets separate these three flows, as shown in the figure. All the flow velocities are assumed to be subsonic, and for simplicity we assume that the sound speeds and mean densities of all the flows are constant with $c_1 = c_2 = c_3 = c$

and $\rho_1 = \rho_2 = \rho_3 = \rho$, respectively. Different ρ or c for different streams could be included in our analysis without substantive modification and might lead to additional phenomena in the solutions. Quantities are non-dimensionalized by c and R_o, so Mach numbers are $M_i = v_i/c$ and the non-dimensional radius of the jet flow is $h = R_i/R_o$.

2.1. *Governing equations and boundary conditions*

The mean flow is perturbed by low-amplitude (linear) waves, which in general are the superposition of acoustic waves and instability waves on the vortex sheets. The entire flow field is assumed irrotational except for the vortex sheets. We neglect any viscosity or thermal conductivity. With these assumptions, the flow field can be expressed as a velocity potential $\phi_t(r, \theta, z)$ satisfying advected Helmholtz equations:

$$\left(\frac{\partial}{\partial t} + M_1 \frac{\partial}{\partial z}\right)^2 \phi_t - \Delta\phi_t = 0, \quad r < h, \tag{2.1a}$$

$$\left(\frac{\partial}{\partial t} + M_2 \frac{\partial}{\partial z}\right)^2 \phi_t - \Delta\phi_t = 0, \quad h < r < 1, \tag{2.1b}$$

$$\left(\frac{\partial}{\partial t} + M_3 \frac{\partial}{\partial z}\right)^2 \phi_t - \Delta\phi_t = 0, \quad r > 1. \tag{2.1c}$$

The subscript t in ϕ_t indicates the total field, in contrast to ϕ without subscript, which we introduce later to indicate the scattered field.

The boundary conditions are the following:

(i) The normal velocity vanishes at the shroud walls, so

$$\frac{\partial \phi_t}{\partial r}(1^-, \theta, z) = \frac{\partial \phi_t}{\partial r}(1^+, \theta, z) = 0, \quad z \leqslant 0. \tag{2.2}$$

(ii) The outer vortex sheet satisfies the usual kinematic condition:

$$\left(\frac{\partial}{\partial t} + M_2 \frac{\partial}{\partial z}\right)\eta(\theta, z) = \frac{\partial \phi_t}{\partial r}(1^-, \theta, z), \quad z > 0, \tag{2.3a}$$

$$\left(\frac{\partial}{\partial t} + M_3 \frac{\partial}{\partial z}\right)\eta(\theta, z) = \frac{\partial \phi_t}{\partial r}(1^+, \theta, z), \quad z > 0, \tag{2.3b}$$

where $\eta(\theta, z)$ is the radial displacement of the sheet.

(iii) The usual dynamic condition requires the pressure to be continuous across the vortex sheets. For the outer vortex sheet this leads to

$$\left(\frac{\partial}{\partial t} + M_2 \frac{\partial}{\partial z}\right)\phi_t(1^-, \theta, z, t) = \left(\frac{\partial}{\partial t} + M_3 \frac{\partial}{\partial z}\right)\phi_t(1^+, \theta, z, t), \quad z > 0. \tag{2.4}$$

(iv) The corresponding kinematic and dynamic boundary conditions applied to the inner vortex sheet are

$$\left(\frac{\partial}{\partial t} + M_1 \frac{\partial}{\partial z}\right)\zeta(\theta, z) = \frac{\partial \phi_t}{\partial r}(h^-, \theta, z), \quad -\infty < z < \infty, \tag{2.5a}$$

$$\left(\frac{\partial}{\partial t} + M_2 \frac{\partial}{\partial z}\right)\zeta(\theta, z) = \frac{\partial \phi_t}{\partial r}(h^+, \theta, z), \quad -\infty < z < \infty, \tag{2.5b}$$

where $\zeta(\theta, z)$ is the radial displacement of the inner sheet,

and (v)

$$\left(\frac{\partial}{\partial t} + M_1 \frac{\partial}{\partial z}\right)\phi_t(h^-, \theta, z, t) = \left(\frac{\partial}{\partial t} + M_2 \frac{\partial}{\partial z}\right)\phi_t(h^+, \theta, z, t), \quad -\infty < z < \infty. \tag{2.6}$$

(vi) At the shroud edge, a full Kutta condition is applied. This condition requires all the available vorticity to be shed from the tip, where the instability wave is parallel to the trailing edge at $z = 0$. Mathematically, this means $\partial\eta/\partial z = 0$ $(r = 1, z = 0)$, which from (2.3) leads to

$$\phi_t(1, z) = O\left(z^{3/2}\right) \qquad \text{as} \quad z \to 0^+, \tag{2.7}$$

ensuring that pressure is also finite at the edge. The condition for no vortex shedding at the shroud tip is

$$\phi_t(1, z) = O\left(z^{1/2}\right) \qquad \text{as} \quad z \to 0^+, \tag{2.8}$$

which results in a pressure singularity at the edge. We will consider this case briefly in §6.2.3 for purposes of comparison.

(vii) A radiation condition applies at infinity, but this is difficult to enforce in a way that suppresses spurious non-Kelvin–Helmholtz modes which are known to exist (Crow & Champagne 1971; Lee & Jones 1973). Instead, they are typically suppressed via a generalized causality statement. For a time dependence of $\exp(-i\omega t)$, ω must be complex with a positive imaginary part: $\omega = \omega_r + i\omega_i = |\omega|\exp(i\delta)$, $0 \leqslant \delta \leqslant \pi/2$. A theorem of Jones & Morgan (1974) shows that causality is then ensured for all possible disturbances for large ω_i and thus $\delta \to \pi/2$. Radiation is effectively satisfied as a consequence. There is a continuum of such causal solutions, but only one of them satisfies the full Kutta condition (Crighton & Leppington 1974). This particular solution must include instability waves.

2.2. *Incident and scattered fields*

The equations of §2.1 are to be solved for scattered (acoustic) waves for different incident (acoustic or vortex sheet) waves, which requires the usual decomposition of the total field ϕ_t into incident ϕ_i and scattered fields ϕ:

$$\phi_t = \phi_i + \phi. \tag{2.9}$$

Assuming harmonic time dependence $\exp(-i\omega t)$ and azimuthal dependence $\exp(-im\theta)$, the general scattered field inside a corresponding infinite shroud is

$$\phi(r, \theta, z, t) = \sum_{m=-\infty}^{\infty} \sum_{n=1}^{\infty} [B_{mn}^+ \exp(i\mu_{mn}^+ \omega z) + B_{mn}^- \exp(i\mu_{mn}^- \omega z)] \Psi_{mn}(r) \exp\{i(m\theta - \omega t)\}. \tag{2.10}$$

It has both left $(-)$ and right $(+)$ moving components. The amplitudes $B_{mn}^\pm$, the axial wavenumbers $\mu_{mn}^\pm$, and the mode shapes Ψ_{mn} will be determined for specific incident and reflected waves in §4 and §6. In (2.10), the axisymmetric modes are given by $(0, n)$, with the plane wave giving $\Psi_{01} = 1$. The non-axisymmetric mode cases have $m \neq 0$. Enforcing the same θ and t dependence on the displacements of the two shear layers yields

$$\eta(\theta, z, t) = \xi(z) \exp\{i(m\theta - \omega t)\}, \tag{2.11a}$$

$$\zeta(\theta, z, t) = \gamma(z) \exp\{i(m\theta - \omega t)\}. \tag{2.11b}$$

The incident wave ϕ_i is taken to be a right-propagating mode (m, n). For the acoustic type incident wave case, since it originates from the inside of the shroud, it is best defined as a solution of the corresponding infinite, co-flowing shroud. It satisfies (2.1) and the wall and the inner shear layer boundary conditions: (i), (iv) and (v)

in §2.1. The incident wave is thus

$$\phi_i(r, \theta, z, t) = \begin{cases} B_{mn}^+ \Psi_{mn}(r) \exp(i\omega\mu_{mn}^+ z + im\theta - i\omega t) & \text{for} \quad r < 1, \\ 0 & \text{for} \quad r > 1. \end{cases} \tag{2.12}$$

In this case, the total field ϕ_t from (2.9), on applying the harmonic time and azimuthal dependence, can be rewritten as

$$\phi_t(r, \theta, z, t) = [\psi_i(r, z) + \psi(r, z)]\exp\{i(m\theta - \omega t)\}, \tag{2.13}$$

with

$$\psi_i(r, z) = B_{mn}^+ \Psi_{mn}(r)\exp(i\omega\mu_{mn}^+ z). \tag{2.14}$$

A more complex approach is necessary to identify incident waves on the inner vortex sheet, which is developed in detail in §4.2. However, in the end these waves are also of the general form (2.14), so both acoustic and vorticity incident waves can be formulated within a single framework as in the following.

Upon using (2.11), (2.13) and (2.14) and suppressing $\exp\{i(m\theta - \omega t)\}$, (2.1)–(2.7) become

$$\frac{\partial^2 \psi}{\partial z^2} + \frac{1}{r}\frac{\partial}{\partial r}\left(r\frac{\partial \psi}{\partial r}\right) - \frac{m^2}{r^2}\psi - \left(-i\omega + M_1\frac{\partial}{\partial z}\right)^2 \psi = 0 \quad \text{for} \quad r < h, \tag{2.15a}$$

$$\frac{\partial^2 \psi}{\partial z^2} + \frac{1}{r}\frac{\partial}{\partial r}\left(r\frac{\partial \psi}{\partial r}\right) - \frac{m^2}{r^2}\psi - \left(-i\omega + M_2\frac{\partial}{\partial z}\right)^2 \psi = 0 \quad \text{for} \quad h < r < 1, \tag{2.15b}$$

$$\frac{\partial^2 \psi}{\partial z^2} + \frac{1}{r}\frac{\partial}{\partial r}\left(r\frac{\partial \psi}{\partial r}\right) - \frac{m^2}{r^2}\psi - \left(-i\omega + M_3\frac{\partial}{\partial z}\right)^2 \psi = 0 \quad \text{for} \quad r > 1; \tag{2.15c}$$

$$\frac{\partial \psi}{\partial r}(1^-, z) = \frac{\partial \psi}{\partial r}(1^+, z) = 0 \quad \text{for} \quad z \leqslant 0, \tag{2.16}$$

$$\left(-i\omega + M_2\frac{\partial}{\partial z}\right)\xi(z) = \frac{\partial \psi}{\partial r}(1^-, z) \quad \text{for} \quad z > 0, \tag{2.17a}$$

$$\left(-i\omega + M_3\frac{\partial}{\partial z}\right)\xi(z) = \frac{\partial \psi}{\partial r}(1^+, z) \quad \text{for} \quad z > 0, \tag{2.17b}$$

$$\left(-i\omega + M_2\frac{\partial}{\partial z}\right)[\psi(1^-, z) + \psi_i(1^-, z)] = \left(-i\omega + M_3\frac{\partial}{\partial z}\right)\psi(1^+, z) \quad \text{for} \quad z > 0, \tag{2.18}$$

$$\left(-i\omega + M_1\frac{\partial}{\partial z}\right)\gamma(z) = \frac{\partial \psi}{\partial r}(h^-, z) \quad \text{for} \quad -\infty < z < \infty, \tag{2.19a}$$

$$\left(-i\omega + M_2\frac{\partial}{\partial z}\right)\gamma(z) = \frac{\partial \psi}{\partial r}(h^+, z) \quad \text{for} \quad -\infty < z < \infty, \tag{2.19b}$$

$$\left(-i\omega + M_1\frac{\partial}{\partial z}\right)\psi(h^-, z) = \left(-i\omega + M_2\frac{\partial}{\partial z}\right)\psi(h^+, z) \quad \text{for} \quad -\infty < z < \infty, \tag{2.20}$$

$$\psi(1, z) = O\left(z^{3/2}\right) \quad \text{as} \quad z \to 0^+. \tag{2.21}$$

3. Wiener–Hopf solution of the scattered field

In this section we develop the Wiener–Hopf solution of (2.15)–(2.21) for a generic incident mode. In the following section, §4, specific formulations for acoustic and

vortical incident waves are developed. A brief summary of the technique is as follows. First, appropriate half-range Fourier transforms are defined in the axial z-direction and applied to the governing equations and boundary conditions (see § 3.1). For all values of r, the transformed functions are analytic inside a strip S in the complex plane. These transformed expressions are then manipulated algebraically to form the so-called Wiener–Hopf equation (3.21). Each of the variables and functions in this equation are then split into two parts (the 'plus' and 'minus' parts) that are analytic in the respective half-planes (see § 3.3), which facilitates construction of a function that is analytic in the whole complex plane. The solution is the inverse transform of this function (see § 3.3).

3.1. *Fourier transforms*

The half-range Fourier transform of any function $f(r, z)$ is

$$\hat{f}^{\pm}(r, s) = \int_{-\infty}^{+\infty} f(r, z) H(\pm z) \exp(-\mathrm{i}\omega s z) \, \mathrm{d}z, \tag{3.1}$$

where $H(z)$ is the Heaviside step function. The inverse transform is

$$f(r, z) = \frac{\omega}{2\pi} \int_{-\infty}^{+\infty} \hat{f}(r, s) \exp(\mathrm{i}\omega s z) \, \mathrm{d}s, \tag{3.2}$$

where

$$\hat{f} = \hat{f}^{+} + \hat{f}^{-}. \tag{3.3}$$

Applying (3.1) and (3.3) to (2.15) yields three Bessel equations:

$$\frac{1}{r} \frac{\partial}{\partial r} \left(r \frac{\partial \hat{\psi}}{\partial r} \right) + \left(\omega^2 \lambda_1^2 - \frac{m^2}{r^2} \right) \hat{\psi} = 0 \quad \text{for} \quad r < h, \tag{3.4a}$$

$$\frac{1}{r} \frac{\partial}{\partial r} \left(r \frac{\partial \hat{\psi}}{\partial r} \right) + \left(\omega^2 \lambda_2^2 - \frac{m^2}{r^2} \right) \hat{\psi} = 0 \quad \text{for} \quad h < r < 1, \tag{3.4b}$$

$$\frac{1}{r} \frac{\partial}{\partial r} \left(r \frac{\partial \hat{\psi}}{\partial r} \right) + \left(\omega^2 \lambda_3^2 - \frac{m^2}{r^2} \right) \hat{\psi} = 0 \quad \text{for} \quad r > 1, \tag{3.4c}$$

where the radial wavenumbers λ_1, λ_2 and λ_3 are defined as $\lambda_p = \lambda_p^+ \lambda_p^-$ for

$$\lambda_p^{\pm} = [1 - s(M_p \pm 1)]^{1/2} \quad \text{for} \quad p = 1, 2, 3. \tag{3.5}$$

The principal branch cuts of the square roots in (3.5) are chosen such that $\mathrm{Im}\,[\lambda_p] > 0$ for $s \to +\infty$. This is ensured by defining cuts from s_p^+ to ∞ along the positive real s-axis and from s_p^- to $-\infty$ along the negative real s-axis with

$$s_p^{\pm} = 1/(M_p \pm 1) \quad \text{for} \quad p = 1, 2, 3. \tag{3.6}$$

The overlapping half-planes R^+ and R^-, in which the respective Fourier transforms (3.1) are analytic can be obtained from these definitions for any δ as

$$R_1^{\pm} : \pm\mathrm{Im}(s - s_1^{\pm}) < \mp \,\mathrm{Re}(s - s_1^{\pm}) \tan \delta \quad \text{for} \quad r < h, \tag{3.7a}$$

$$R_2^{\pm} : \pm\mathrm{Im}(s - s_2^{\pm}) < \mp \,\mathrm{Re}(s - s_2^{\pm}) \tan \delta \quad \text{for} \quad h < r < 1, \tag{3.7b}$$

$$R_3^{\pm} : \pm\mathrm{Im}(s - s_3^{\pm}) < \mp \,\mathrm{Re}(s - s_3^{\pm}) \tan \delta \quad \text{for} \quad r > 1. \tag{3.7c}$$

The domain of regularity of the transformed functions is at the intersection of these six half-planes, S, as shown in figure 3. For subsonic $M_1 > M_2 > M_3$, the boundaries
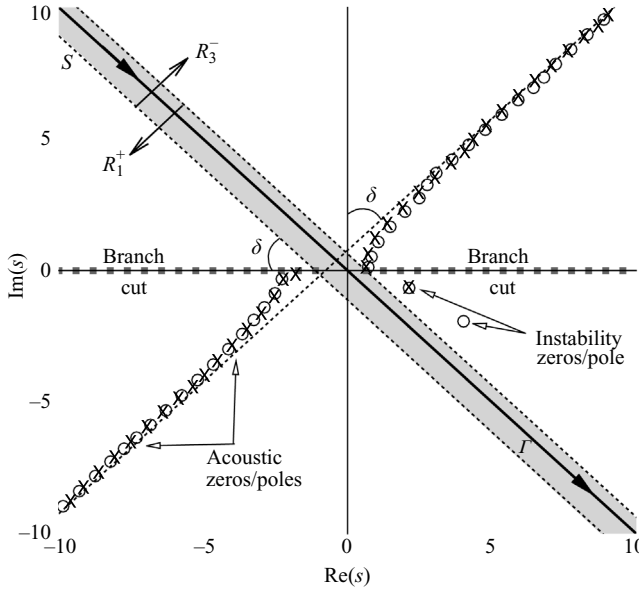
FIGURE 3. The zeros ($\circ$) and poles ($\times$) of the kernel given by (3.22) are shown for $\delta = \pi/4$. The parameters are $M_1 = 0.55$, $M_2 = 0.3$, $M_3 = 0.1$, $h = 0.9$, $\omega = 5$, and $m = 1$. Also note the definitions of the R_1^+ and R_3^- half-planes, the inverse Fourier transform contour Γ and the shaded strip S.

of S are set by R_1^+ and R_3^-. An acceptable inverse Fourier transform path lies in S along Γ defined by $\arg s = \delta$.

A general solution of (3.4) for $p = 1, 2, 3$ is

$$\hat{\psi}(r, s) = A_p(s)\mathrm{J}_m(\lambda_p \omega r) + B_p(s)\mathrm{H}_m^{(1)}(\lambda_p \omega r), \tag{3.8}$$

where J_m and $\mathrm{H}_m^{(1)}$ are respectively the order-m Bessel and Hankel functions of the first kind. Setting $B_1 = 0$ ensures regular behaviour of $\hat{\psi}$ as $r \to 0$. Similarly, setting $A_3 = 0$ ensures radiation at infinity given that $\mathrm{Im}\,[\lambda_3 \omega]$ in S is positive, for the definitions of the radial wavenumbers and their branch cuts used in the analysis. Thus, the solution of (3.4) is

$$\hat{\psi}(r, s) = \begin{cases} A_1(s)\mathrm{J}_m(\lambda_1 \omega r) & \text{for } r < h, \\ A_2(s)\mathrm{J}_m(\lambda_2 \omega r) + B_2(s)\mathrm{H}_m^{(1)}(\lambda_2 \omega r) & \text{for } h < r < 1, \\ B_3(s)\mathrm{H}_m^{(1)}(\lambda_3 \omega r) & \text{for } r > 1. \end{cases} \tag{3.9}$$

The undetermined constants in (3.9) are found by Fourier transforming the boundary conditions. The transformed vortex sheet displacements, $\hat{\xi}^+(s)$ and $\hat{\gamma}(s)$, corresponding to the outer and inner shear layers, are defined according to (3.1). The outer sheet exists only for $z > 0$, and thus only has the 'plus' transformed part of $\hat{\xi}$. In addition, for convenience, two other quantities are defined that correspond to the pressure jump across the vortex sheets. These jumps are in the scattered pressures; the total pressure is, of course, continuous across the sheets. By the definition of scattered pressure in (2.18) and (2.20) these jumps are

$$\hat{p}_o(s) = \int_{-\infty}^{+\infty} \left[\left(-\mathrm{i}\omega + M_3 \frac{\partial}{\partial z}\right)\psi(1^+, z) - \left(-\mathrm{i}\omega + M_2 \frac{\partial}{\partial z}\right)\psi(1^-, z) \right] \exp(-\mathrm{i}\omega s z)\mathrm{d}z \tag{3.10}$$

for the outer shear layer ($z > 0$) and the shroud walls ($z < 0$) and

$$\hat{p}_i(s) = \int_{-\infty}^{+\infty} \left[\left(-\mathrm{i}\omega + M_2 \frac{\partial}{\partial z} \right) \psi(h^+, z) - \left(-\mathrm{i}\omega + M_1 \frac{\partial}{\partial z} \right) \psi(h^-, z) \right] \exp(-\mathrm{i}\omega s z) \mathrm{d}z \quad (3.11)$$

for the inner shear layer ($-\infty < z < \infty$). Applying (3.9) to (3.10) and (3.11) yields

$$\hat{p}_o(s) = -\mathrm{i}\omega \big\{ (1 - sM_3) \, B_3(s) \, \mathrm{H}_m^{(1)}(\lambda_3\omega)$$
$$- (1 - sM_2) \, [A_2(s) \, \mathrm{J}_m(\lambda_2\omega) + B_2(s) \, \mathrm{H}_m^{(1)}(\lambda_2\omega)] \big\}, \quad (3.12)$$

and

$$\hat{p}_i(s) = -\mathrm{i}\omega \big\{ (1 - sM_2) \, [A_2(s) \, \mathrm{J}_m(\lambda_2\omega h) + B_2(s) \, \mathrm{H}_m^{(1)}(\lambda_2\omega h)]$$
$$- (1 - sM_1) \, A_1(s) \, \mathrm{J}_m(\lambda_1\omega h) \big\}. \quad (3.13)$$

Taking a similar approach, applying (3.9) to (2.17) and using (2.16), the Fourier transform of the kinematic boundary condition on the outer vortex sheet (2.17) becomes

$$-\mathrm{i}(1 - sM_2)\hat{\xi}^+(s) = \lambda_2 \{ A_2(s)\mathrm{J}'_m(\lambda_2\omega) + B_2(s)\mathrm{H}_m^{(1)\prime}(\lambda_2\omega) \}, \quad (3.14a)$$

$$-\mathrm{i}(1 - sM_3)\hat{\xi}^+(s) = \lambda_3 B_3(s)\mathrm{H}_m^{(1)\prime}(\lambda_3\omega). \quad (3.14b)$$

Here primes denote derivative with respect to the argument of the function. The inner shear layer displacement given by (2.19) can similarly be transformed to

$$-\mathrm{i}(1 - sM_1)\hat{\gamma}(s) = \lambda_1 \{ A_1(s)\mathrm{J}'_m(\lambda_1\omega h) \}, \quad (3.15a)$$

$$-\mathrm{i}(1 - sM_2)\hat{\gamma}(s) = \lambda_2 \{ A_2(s)\mathrm{J}'_m(\lambda_2\omega h) + B_2(s)\mathrm{H}_m^{(1)\prime}(\lambda_2\omega h) \}. \quad (3.15b)$$

The Fourier transform of the dynamic boundary condition on the outer vortex sheet (2.18) with application of (3.10) and (2.14) leads to

$$\hat{p}_o^+(s) = B_{mn}^+ \Psi_{mn}(1) \frac{1 - \mu_{mn}^+ M_2}{\mu_{mn}^+ - s}. \quad (3.16)$$

The corresponding transform of (2.20) using (3.11) reduces to

$$\hat{p}_i(s) = 0, \quad (3.17)$$

as it must since for the inner shear layer both the total pressures and the scattered pressures are continuous for our choices of incident waves.

To determine the constants in (3.9), we sequentially combine (3.13), (3.17), (3.15), and (3.14) to arrive at

$$A_1(s) = -\frac{\mathrm{i}}{\lambda_2} \frac{(1 - sM_2)^2}{1 - sM_1} \frac{\hat{\xi}^+(s)}{\mathrm{J}_m(\lambda_1\omega h)} \frac{\mathrm{H}_m^{(1)}(\lambda_2\omega h) + R(s)\mathrm{J}_m(\lambda_2\omega h)}{\mathrm{H}_m^{(1)\prime}(\lambda_2\omega) + R(s)\mathrm{J}'_m(\lambda_2\omega)}, \quad (3.18a)$$

$$A_2(s) = -\frac{\mathrm{i}}{\lambda_2}(1 - sM_2) \frac{\hat{\xi}^+(s)R(s)}{\mathrm{H}_m^{(1)\prime}(\lambda_2\omega) + R(s)\mathrm{J}'_m(\lambda_2\omega)}, \quad (3.18b)$$

$$B_2(s) = -\frac{\mathrm{i}}{\lambda_2}(1 - sM_2) \frac{\hat{\xi}^+(s)}{\mathrm{H}_m^{(1)\prime}(\lambda_2\omega) + R(s)\mathrm{J}'_m(\lambda_2\omega)}, \quad (3.18c)$$

$$B_3(s) = -\frac{\mathrm{i}}{\lambda_3}(1 - sM_3) \frac{\hat{\xi}^+(s)}{\mathrm{H}_m^{(1)\prime}(\lambda_3\omega)}, \quad (3.18d)$$

where we have defined

$$R(s) = \frac{\lambda(s)J_m(\lambda_1\omega h)H_m^{(1)\prime}(\lambda_2\omega h) - H_m^{(1)}(\lambda_2\omega h)J_m^\prime(\lambda_1\omega h)}{J_m(\lambda_2\omega h)J_m^\prime(\lambda_1\omega h) - \lambda(s)J_m(\lambda_1\omega h)J_m^\prime(\lambda_2\omega h)}, \tag{3.19}$$

with

$$\lambda(s) = \frac{\lambda_2}{\lambda_1}\frac{(1-sM_1)^2}{(1-sM_2)^2}. \tag{3.20}$$

The one remaining unknown in (3.18) is $\hat{\xi}^+$, the Fourier transform of the outer vortex sheet displacement. To determine $\hat{\xi}^+$ we substitute (3.18b)–(3.18d) into (3.12) and utilize $\hat{p}_o = \hat{p}_o^+ + \hat{p}_o^-$ to arrive at

$$K(s)\hat{\xi}^+(s) - \hat{p}_o^+(s) = \hat{p}_o^-(s), \tag{3.21}$$

where $\hat{p}_o^+$ is given by (3.16). This manipulation introduces $\hat{p}_o^-$, the pressure jump across the shroud wall, as a second unknown. Equation (3.21) is the Wiener–Hopf equation with kernel

$$K(s) = \omega\left\{\frac{(1-sM_2)^2}{\lambda_2}\left[\frac{H_m^{(1)}(\lambda_2\omega) + R(s)J_m(\lambda_2\omega)}{H_m^{(1)\prime}(\lambda_2\omega) + R(s)J_m^\prime(\lambda_2\omega)}\right] - \frac{(1-sM_3)^2}{\lambda_3}\frac{H_m^{(1)}(\lambda_3\omega)}{H_m^{(1)\prime}(\lambda_3\omega)}\right\}. \tag{3.22}$$

Though not obvious as formulated, the kernel so-obtained is equivalent to the one obtained by Taylor *et al.* (1993) in their 'plane B sub-problem', which they solve for acoustic interactions in the low-frequency limit. We use it to obtain scattering solutions for finite-wavelength acoustic and vorticity incident waves.

3.2. *The kernel*

The poles and zeros of the kernel define the characteristics of the problem, the exact locations of which depend upon the parameters chosen. Since the analysis and the subsequent contour integrations depend upon the locations of these zeros/poles, it is important to identify their characteristics (e.g. acoustic or instability modes) and locations. Figure 3 shows the poles and zeros of (3.22) for one set of parameters. There are two basic types of zeros and poles. The first correspond to the acoustic shroud modes and these zeros and poles lie along a curve that asymptotically approaches $\pi/2 - \delta$ for large $|s|$. The acoustic poles come from the denominators of (3.22), and most of them come from the first term. Since this first term's denominator corresponds to the characteristic equation of the infinite shroud (see (4.3)), poles from this denominator match the acoustic modes of an infinite shroud. From figure 4(*b*), it is clear that the second-term denominator contributes only two poles for all parameters investigated. This second term of (3.22) can be thought of as a correction term that accounts for finite termination of the infinite shroud, as evidenced by M_3 appearing only in this term. The poles lying on the real axis for $\delta \rightarrow 0$ (figure 4*a*) correspond to propagating waves, whereas the disturbances associated with the rest decay away from the shroud exit. In §4 and §6, where we select specific incident and reflected waves, we focus on these propagating waves. Nevertheless, for a short distance between the shroud exit and the nozzle lip upstream of it, some of the decaying acoustic components of the reflected wave may be important.

The second type of poles and zeros corresponds to the Helmholtz instability modes of the vortex sheets. These zeros and pole sit in the fourth quadrant of the complex plane, as seen in figure 3. The two zeros correspond to modes of the shear layers downstream of the shroud exit, and the pole corresponds to that of the inner shear layer upstream of the exit. Unlike the low-frequency case considered by Taylor *et al.*
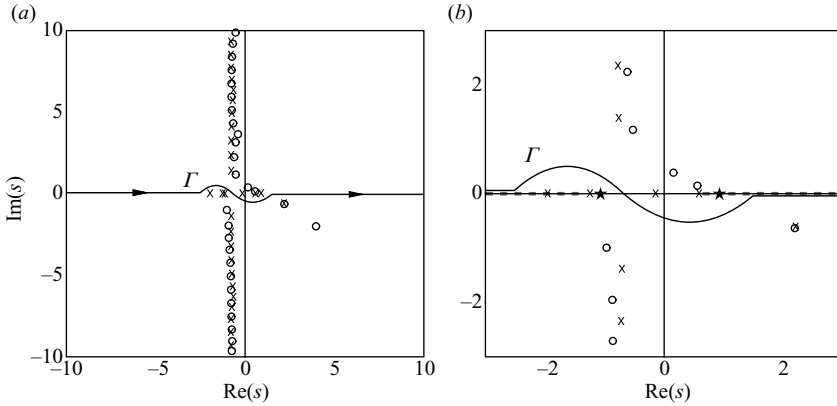
FIGURE 4. (*a*) Example locations of the zeros (○) and poles (×) of $K(s)$ in (3.22) for $\delta \to 0$. (*b*) Enlarged view of (*a*) which in addition identifies ⋆, the poles arising from the second term in (3.22) (see text). Parameters are same as in figure 3.

(1993), for disturbances considered here with wavelengths comparable to the shroud diameter or shorter, the zero and the pole for the inner shear layer are close to each other. This is because of the exponential decay of the disturbances away from the vortex sheet. For moderate wavelengths they only interact weakly with the shroud walls and the instabilities are nearly the same regardless of their confinement. Though weak, this interaction is still important from the perspective of generating sound.

We use a Newton–Raphson iterative scheme to compute these zeros and poles with the derivatives computed using a scheme by Ridders (1982). The close lying zero–pole pairs require good initial estimates.

3.3. *General solutions*

A multiplicative split of the kernel (3.22) can be carried out as $K(s) = K^+(s)K^-(s)$, where the two factors K^+ and K^- are analytic, non-zero and have at most algebraic growth in their respective half-planes. However, it is more convenient to factor the instability zeros s_{z_1} and s_{z_2} and the pole s_p out of the kernel before splitting it (e.g. Gabard & Astley 2006). This facilitates the application of the residue theorem in determining the instability part of the scattered solutions (see (3.36), (3.37)). Accordingly, for incident acoustic waves we take

$$K(s) = \tilde{K}^+(s)\tilde{K}^-(s)U(s), \qquad (3.23)$$

where

$$U(s) = \left(s - s_{z_1}\right)\left(s - s_{z_2}\right)/(s - s_p). \qquad (3.24)$$

For an incident vorticity wave, the inner vortex sheet pole acts as the incident mode, so streamwise wavenumber μ_{mn}^+ from (2.14) is $\mu_{mn}^+ = s_p$. Using (3.24) in this case to compute terms such as $\tilde{K}^-(\mu_{mn}^+)$ from (A 1) in the Appendix and (3.23), as needed later in (3.30), is numerically problematic, as $U(\mu_{mn}^+)$ becomes singular. It is then best not to factor out s_p as in (3.24). Given the close proximity of s_{z_1} and s_p it is also best to leave s_{z_1} unfactored. The kernel integration contour C (see Appendix A.1) is simply deformed around both. Thus for the incident vorticity case

$$U(s) = \left(s - s_{z_2}\right). \qquad (3.25)$$

In both cases, $\tilde{K}^+$ and $\tilde{K}^-$ are split functions of K/U. Substituting (3.23) into (3.21) yields

$$U(s)\tilde{K}^+(s)\hat{\xi}^+(s) - \frac{\hat{p}_o^+(s)}{\tilde{K}^-(s)} = \frac{\hat{p}_o^-(s)}{\tilde{K}^-(s)}. \tag{3.26}$$

The first term on the left-hand side is analytic in R^+, whereas the right-hand-side term is analytic in R^-. Unfortunately, $\hat{p}_o^+$ has a pole at $s = \mu_{mn}^+$ (see (3.16)) so that the second term is not analytic in R^-. This is resolved by the rearrangement

$$U(s)\tilde{K}^+(s)\hat{\xi}^+(s) - \frac{\hat{p}_o^+(s)}{\tilde{K}^-(\mu_{mn}^+)} = \frac{\hat{p}_o^-(s)}{\tilde{K}^-(s)} + \hat{p}_o^+(s)\left[\frac{1}{\tilde{K}^-(s)} - \frac{1}{\tilde{K}^-(\mu_{mn}^+)}\right]. \tag{3.27}$$

Since $\tilde{K}^-$ is analytic in R^-, $\tilde{K}^-(\mu_{mn}^+)$ is just a finite constant, so the entire left-hand side is regular in R^+. Also, the singularity that $\hat{p}_o^+$ had in R^- is cancelled by the corresponding zero of the bracketed term on the right. This second term on the right-hand side is thus appropriately analytic in R^-. As formulated, (3.27) is regular in S, so by the usual analyticity arguments each side is equal to some common function that is analytic in the entire complex s-plane.

By the extended Liouville's theorem (e.g. Noble 1988), which requires such functions to be polynomials, we have

$$U(s)\tilde{K}^+(s)\hat{\xi}^+(s) - \frac{\hat{p}_o^+(s)}{\tilde{K}^-(\mu_{mn}^+)} = \frac{\hat{p}_o^-(s)}{\tilde{K}^-(s)} + \hat{p}_o^+(s)\left[\frac{1}{\tilde{K}^-(s)} - \frac{1}{\tilde{K}^-(\mu_{mn}^+)}\right]$$
$$= \sum_{k=0}^{N} a_k s^k \quad \text{as} \quad |s| \to \infty. \tag{3.28}$$

The next step is to use the asymptotic forms of the above expressions to determine the a_k in the sum. All the terms in (3.28) must have the same behaviour for large $|s|$, so we consider only the first term, which is the easiest to analyse. Asymptotic forms of certain sub-components of (3.22) are provided in the Appendix, §A.2. To find $\tilde{K}^+(s)$ for large $|s|$, we start by considering $K(s)$. In the strip S, $\lambda_3\omega$ has a positive imaginary part (see the argument made before (3.9)), so for $|s| \to \infty$ the Hankel function ratio involving M_3 in (3.22) is negative (using (A3)), and thus $K(s)$ can be approximated as $K(s) \approx (1 - sM_2)^2/\lambda_2 + (1 - sM_3)^2/\lambda_3$. This gives $K(s) \sim s$ for large $|s|$ in S. From (3.24) and (3.25) we have $U(s) \sim s$ as $|s| \to \infty$. Thus $K(s)/U(s) \sim 1$ as $|s| \to \infty$, which gives $\tilde{K}^+(s) = \tilde{K}^-(s) \sim 1$, with the phase remaining the same, as $|s| \to \infty$. To find the large-$|s|$ behaviour of $\hat{\xi}^+(s)$, we use the Kutta condition (2.21) and the definition of the Fourier transform (3.1), which gives $\hat{\psi}(1, s) \sim s^{-5/2}$. Using this in (3.9) for $r > 1$ indicates that $B_3(s) \sim s^{-5/2}$, since $\text{Im}[\lambda_3\omega] > 0$. Also, since $\lambda_3(s) \sim s$ as $|s| \to \infty$ by (3.5), from (3.14b) we conclude that $\hat{\xi}^+(s) \sim s^{-5/2}$ as $|s| \to \infty$. Thus

$$U(s)\tilde{K}^+(s)\hat{\xi}^+(s) \sim s^{1+0-5/2} \sim s^{-3/2} \quad \text{as} \quad |s| \to \infty. \tag{3.29}$$

This requires $a_k = 0$, for all k, in (3.28), which upon application of (3.16) yields

$$\hat{\xi}^+(s) = B_{mn}^+ \Psi_{mn}(1)\frac{1 - \mu_{mn}^+ M_2}{(\mu_{mn}^+ - s)\tilde{K}^-(\mu_{mn}^+)\tilde{K}^+(s)U(s)}. \tag{3.30}$$

The same procedure may be repeated using (2.8) to obtain the no-vortex-shedding solution. Introducing the complex vortex shedding parameter γ used by Gabard &
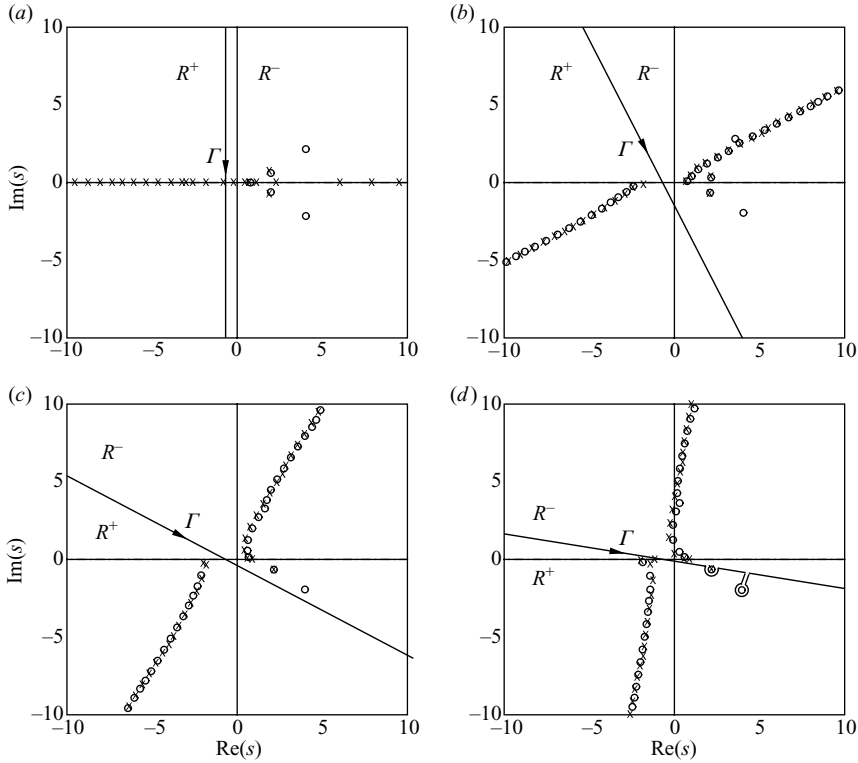
FIGURE 5. The zeros (○) and the poles (×) of (3.22) in the complex plane as δ changes from $\delta \to \pi/2$ to $\delta \to 0$. The parameters are the same as in figure 3 with (a) $\delta = \pi/2$, (b) $\pi/3$, (c) $\pi/6$ and (d) $\pi/18$. Note how the instability zeros and pole lying in the fourth quadrant tend to move from R^- to R^+ between (c) and (d) which requires deformation of Γ. Also, the complex conjugates of the instability zeros/pole can be seen in (a), which correspond to decaying convective instability modes and are not included in the analysis.

Astley (2006) and Rienstra (1984) generalizes (3.30) to

$$\hat{\xi}^+(s) = B_{mn}^+ \Psi_{mn}(1) \frac{1 - \mu_{mn}^+ M_2}{(\mu_{mn}^+ - s_{z_2})\tilde{K}^-(\mu_{mn}^+)\tilde{K}^+(s)U(s)} \left(\frac{s - s_{z_2}}{\mu_{mn}^+ - s} + \gamma \right), \qquad (3.31)$$

where $0 < |\gamma| < 1$. The special cases are $\gamma = 1$, which reduces to (3.30) and is the full Kutta condition, and $\gamma = 0$, the no-vortex-shedding condition.

The physical solutions we seek are for real-valued ω, which corresponds to $\delta \to 0$. This rotates the inverse transform contour Γ in figure 5(a), to be parallel to the real axis (see figure 4a). As a result Γ now extends from $-\infty + 0\mathrm{i}$ to $\infty - 0\mathrm{i}$, crossing the real s-axis at some intermediate point so that analytic continuity is preserved. Figure 5 depicts how the various poles and zeros of the kernel move as $\delta \to 0$. The instability zeros/pole do not move with this rotation and so Γ must be deformed around them to ensure they remain in R^- and analytic continuity is preserved (figure 5d). In practice, however, a simple application of the residue theorem is sufficient to explicitly identify the contribution of these instability modes. We must also be aware of the movement of the acoustic poles and zeros and account for their crossing, if any, as Γ is rotated. In a related problem, Munt (1977) carried out an extensive asymptotic and numerical analysis to locate the kernel zeros and poles for a wide range of flow parameters and different δ to conclude that the acoustic zeros/poles do not cross Γ

as $\delta \to 0$. Such an analysis is intractable in cases like the present (e.g. Taylor *et al.* 1993). However, we have made careful observations of the movement of acoustic zeros/poles as δ varies from $\pi/2$, where causality is satisfied, to $\delta = 0$, to choose Γ. Experiments where a pole/zero was purposely placed on the wrong side of Γ yielded a final solution that clearly violated causality, which also supports our choice of Γ in figure 4(*b*).

The solution of the scattered acoustic potential field is then found by first substituting (3.30) and (3.18) into (3.9) and then using (3.2) to arrive at

$$
\psi_a(r, z) =
\begin{cases}
\dfrac{\omega}{2\pi i} \displaystyle\int_\Gamma \dfrac{(1 - sM_2)^2}{(1 - sM_1)} \dfrac{T_1(r, s)\hat{\xi}^+(s)}{\lambda_2} \exp(i\omega sz)\, ds & \text{for} \quad r < h, \\[4mm]
\dfrac{\omega}{2\pi i} \displaystyle\int_\Gamma (1 - sM_2) \dfrac{T_2(r, s)\hat{\xi}^+(s)}{\lambda_2} \exp(i\omega sz)\, ds & \text{for} \quad h < r < 1, \\[4mm]
\dfrac{\omega}{2\pi i} \displaystyle\int_\Gamma (1 - sM_3) \dfrac{T_3(r, s)\hat{\xi}^+(s)}{\lambda_3} \exp(i\omega sz)\, ds & \text{for} \quad r > 1,
\end{cases}
\tag{3.32}
$$

where

$$
T_1(r, s) = \frac{J_m(\lambda_1 \omega r)}{J_m(\lambda_1 \omega h)} \frac{H_m^{(1)}(\lambda_2 \omega h) + R(s)J_m(\lambda_2 \omega h)}{H_m^{(1)\prime}(\lambda_2 \omega) + R(s)J_m'(\lambda_2 \omega)},
\tag{3.33a}
$$

$$
T_2(r, s) = \frac{H_m^{(1)}(\lambda_2 \omega r) + R(s)J_m(\lambda_2 \omega r)}{H_m^{(1)\prime}(\lambda_2 \omega) + R(s)J_m'(\lambda_2 \omega)},
\tag{3.33b}
$$

$$
T_3(r, s) = \frac{H_m^{(1)}(\lambda_3 \omega r)}{H_m^{(1)\prime}(\lambda_3 \omega)}.
\tag{3.33c}
$$

The solution for the scattered pressure is easily found from (3.32) via the linearized unsteady Bernoulli equation,

$$
p = -\left(\frac{\partial \psi}{\partial t} + M\frac{\partial \psi}{\partial z} \right).
\tag{3.34}
$$

Hence, the scattered acoustic pressure field has the following general solution:

$$
p_a(r, z) =
\begin{cases}
\dfrac{\omega^2}{2\pi} \displaystyle\int_\Gamma \dfrac{(1 - sM_2)^2}{\lambda_2} T_1(r, s)\, \hat{\xi}^+(s) \exp(i\omega sz)\, ds & \text{for} \quad r < h, \\[4mm]
\dfrac{\omega^2}{2\pi} \displaystyle\int_\Gamma \dfrac{(1 - sM_2)^2}{\lambda_2} T_2(r, s)\, \hat{\xi}^+(s) \exp(i\omega sz)\, ds & \text{for} \quad h < r < 1, \\[4mm]
\dfrac{\omega^2}{2\pi} \displaystyle\int_\Gamma \dfrac{(1 - sM_3)^2}{\lambda_3} T_3(r, s)\, \hat{\xi}^+(s) \exp(i\omega sz)\, ds & \text{for} \quad r > 1.
\end{cases}
\tag{3.35}
$$

As mentioned above, the instability part of the scattered field is obtained by applying residue theorem for s_{z_1} and s_{z_2}, which appear as simple poles in (3.32) and (3.35) via the $U(s)$ factor in (3.30). For incident vorticity waves, however, since s_{z_1} was not included in (3.25), the scattered field due to the inner vorticity wave is included in (3.32). The expression for the scattered instability potential is
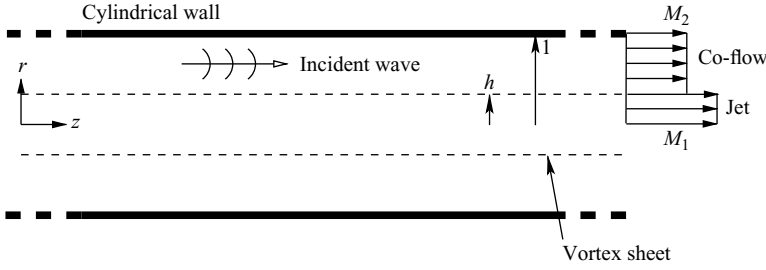
FIGURE 6. Schematic of the infinite shroud with co-flow used to obtain the acoustic incident waves.

then

$$\psi_s(r, z) = \omega \sum_{s'} \exp(\mathrm{i}\omega s' z) \lim_{s \to s'} [\hat{\xi}^+(s)]$$

$$\times H(z) \begin{cases} \dfrac{(1 - s' M_2)^2}{(1 - s' M_1)} \lim_{s \to s'} [T_1(r, s)/\lambda_2] & \text{for} \quad r < h, \\[2mm] (1 - s' M_2) \lim_{s \to s'} [T_2(r, s)/\lambda_2] & \text{for} \quad h < r < 1, \\[2mm] (1 - s' M_3) \lim_{s \to s'} [T_3(r, s)/\lambda_3] & \text{for} \quad r > 1. \end{cases} \tag{3.36}$$

Similarly, the scattered instability pressure is

$$p_s(r, z) = \mathrm{i}\omega^2 \sum_{s'} \exp(\mathrm{i}\omega s' z) \lim_{s \to s'} [\hat{\xi}^+(s)]$$

$$\times H(z) \begin{cases} (1 - s' M_2)^2 \lim_{s \to s'} [T_1(r, s)/\lambda_2] & \text{for} \quad r < h, \\[2mm] (1 - s' M_2)^2 \lim_{s \to s'} [T_2(r, s)/\lambda_2] & \text{for} \quad h < r < 1, \\[2mm] (1 - s' M_3)^2 \lim_{s \to s'} [T_3(r, s)/\lambda_3] & \text{for} \quad r > 1, \end{cases} \tag{3.37}$$

where

$$\lim_{\substack{s \to s' \\ s_i = s'}} [\hat{\xi}^+(s)] = B^+_{mn} \Psi_{mn}(1) \frac{(1 - \mu^+_{mn} M_2)(s' - s_p)}{(\mu^+_{mn} - s') \tilde{K}^-(\mu^+_{mn}) \tilde{K}^+(s')(s' - s_i)}, \tag{3.38}$$

where s' and s_i are respectively s_{z_1} or s_{z_2} or vice versa depending upon which instability wave pressure field is sought. The total scattered potential and pressure are then

$$\psi(r, z) = \psi_a(r, z) + \psi_s(r, z) \quad \text{and} \quad p(r, z) = p_a(r, z) + p_s(r, z), \tag{3.39}$$

with the total field obtained by simply adding the incident field. Though not obvious by visual inspection, it can be confirmed that these solutions degenerate to those of Munt (1977) and Taylor *et al.* (1993) in the appropriate limits (Samanta 2008).

4. Incident waves

We first analyse the acoustic-type incident wave in the following subsection, which has previously been studied only for $m = 0$ in the long-wavelength limit for this configuration. We then take up the instability-type case in §4.2.

4.1. *Acoustic-type incident waves*

In this case the incident waves are the right-propagating modes in an infinite shroud with two concentric streams as shown in figure 6. The starting points are the right-moving + components of (2.10), which were expressed in terms of the unknown

mode shape functions Ψ_{mn}. The governing differential equations (2.15a, b) are satisfied by

$$\Psi_{mn}(r) = \begin{cases} J_m(r\alpha_{mn}), & r < h, \\ \left(\dfrac{1 - \mu_{mn}^+ M_1}{1 - \mu_{mn}^+ M_2}\right) J_m(h\alpha_{mn}) \left[\dfrac{J_m(r\beta_{mn}) H_m^{(1)\prime}(\beta_{mn}) - H_m^{(1)}(r\beta_{mn}) J_m'(\beta_{mn})}{J_m(h\beta_{mn}) H_m^{(1)\prime}(\beta_{mn}) - H_m^{(1)}(h\beta_{mn}) J_m'(\beta_{mn})}\right], & r > h, \end{cases}$$
(4.1)

where for axial wavenumber μ_{mn}^+ the radial wavenumbers

$$\alpha_{mn} = \omega\sqrt{(1 - \mu_{mn}^+ M_1)^2 - \mu_{mn}^{+\,2}} \quad \text{and} \quad \beta_{mn} = \omega\sqrt{(1 - \mu_{mn}^+ M_2)^2 - \mu_{mn}^{+\,2}} \quad (4.2)$$

satisfy the hard wall (2.16) and the dynamic (2.20) boundary conditions. The dispersion relationship, which is obtained via (2.19), provides the final constraint on α, β and μ:

$$\Lambda(z) \equiv z_2(1 - zM_1)^2 J_m(hz_1)[J_m'(hz_2) H_m^{(1)\prime}(z_2) - H_m^{(1)\prime}(hz_2) J_m'(z_2)]$$

$$- z_1(1 - zM_2)^2 J_m'(hz_1)[J_m(hz_2) H_m^{(1)\prime}(z_2) - H_m^{(1)}(hz_2) J_m'(z_2)] = 0, \quad (4.3)$$

with

$$z_1 = \omega\sqrt{(1 - zM_1)^2 - z^2} \quad \text{and} \quad z_2 = \omega\sqrt{(1 - zM_2)^2 - z^2}. \quad (4.4)$$

For any m, the nth real-valued μ_{mn}^+ roots of (4.3) represents the propagating mode (m, n). The requirement that the radial wavenumbers α and β in (4.2) be real valued and positive quantities restricts μ_{mn}^+ as

$$-\frac{1}{1 - M_2} < \mu_{mn}^+ < \frac{1}{1 + M_1}. \quad (4.5)$$

Finally, to be incident on the shroud exit the waves must have non-negative group velocity,

$$\frac{\mathrm{d}\omega}{\mathrm{d}\mu_{mn}^+} > 0. \quad (4.6)$$

The amplitude B_{mn}^+ in (2.14) is taken to be unity for incident acoustic waves.

4.2. *Instability-type incident waves*

Kelvin–Helmholtz instability incident waves satisfy the same equations and boundary conditions as the acoustic modes presented in the last section, but special considerations are warranted to cope with their exponential growth. To construct a finite-amplitude incident wave we must consider a finite-length inner vortex sheet.

We assume that the origin of the instability wave is an inner nozzle lip at a distance z_o upstream of the shroud exit. This upstream distance is assumed to be sufficiently large to decouple the nozzle from the shroud exit. The wavenumber of this instability wave matches s_p defined in (3.24), which is the pole of the kernel (3.22) corresponding to the inner-sheet instability mode. This pole is a zero of the kernel for the configuration shown in figure 7. For incident quasi-plane waves as in Taylor *et al.* (1993), the incident instability wave can be simply obtained from (2.14) since $\Psi_{01}(r) = 1$. The more general incident waves sought here require explicit solutions for $\Psi_{mn}(r)$, which can also be solved using a Wiener–Hopf formulation.

Since a similar problem setup (figure 7) is described in detail by Taylor *et al.* (1993), and extension to finite wavelengths is as discussed in §3 of the present paper for the finite-shroud problem, only a cursory overview is provided here. The governing
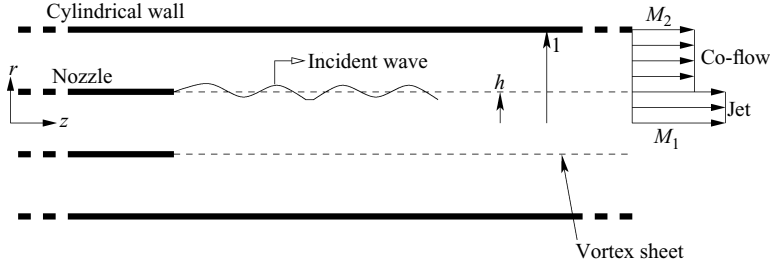
FIGURE 7. Schematic of the infinite shroud with an inner nozzle and co-flow used to obtain the instability incident waves.

equations are the same as (2.1a, b). The wall boundary condition (2.2) is applied to the inner and outer surfaces of the nozzle and the outer, now-infinite, shroud. The usual vortex sheet boundary conditions (2.3) and (2.4), the nozzle-lip Kutta condition (2.7), and the causality requirement complete the problem description. The solution then follows the procedure described in §2.1 and §3, yielding scattered acoustic potential

$$
\psi_a(r, z) =
\begin{cases}
\dfrac{\omega}{2\pi i} \displaystyle\int_\Gamma (1 - sM_1) \dfrac{Y_1(r, s)\hat{\beta}^+(s)}{\lambda_1} \exp(i\omega s z)\, ds & \text{for} \quad r < h, \\[3mm]
\dfrac{\omega}{2\pi i} \displaystyle\int_\Gamma (1 - sM_2) \dfrac{Y_2(r, s)\hat{\beta}^+(s)}{\lambda_2} \exp(i\omega s z)\, ds & \text{for} \quad h < r < 1.
\end{cases}
\tag{4.7}
$$

This is nearly the same as (3.32), but $\hat{\beta}^+(s)$ is the Fourier-transformed vortex sheet displacement for this auxiliary problem and

$$
Y_1(r, s) = \frac{J_m(\lambda_1 \omega r)}{J'_m(\lambda_1 \omega h)},
\tag{4.8a}
$$

$$
Y_2(r, s) = \frac{J_m(\lambda_2 \omega r)H_m^{(1)'}(\lambda_2 \omega) - H_m^{(1)}(\lambda_2 \omega r)J'_m(\lambda_2 \omega)}{J'_m(\lambda_2 \omega h)H_m^{(1)'}(\lambda_2 \omega) - H_m^{(1)'}(\lambda_2 \omega h)J'_m(\lambda_2 \omega)}.
\tag{4.8b}
$$

The transformed vortex sheet displacement is given by

$$
\hat{\beta}^+(s) = \Psi_{mn}(h) \frac{(1 - \mu_{mn}^+ M_1)}{(\mu_{mn}^+ - s)\tilde{K}_1^-(\mu_{mn}^+)\tilde{K}_1^+(s)(s - s_o)}.
\tag{4.9}
$$

Here μ_{mn}^+ is the wavenumber of the acoustic wave incident from inside the nozzle that is used to seed the instability wave in this auxiliary problem. In (4.9), s_o is the zero corresponding to the shear layer instability, which matches the pole s_p for the finite shroud in (3.24), and $\Psi_{mn}(r) = J_m(\alpha_{mn} r)$ with α_{mn} being a solution of $\Lambda(z) = J'_m(z) = 0$. This incident acoustic mode, which only propagates for $\omega > (1 - M_1^2)^{1/2}\alpha_{mn}$ sets a lower bound of $\omega = (1 - M_1^2)^{1/2}\alpha_{m1}$ for the vorticity frequency. The kernel $K_1(s)$ in (4.9) is

$$
K_1(s) = \omega \left\{ \frac{(1 - sM_1)^2}{\lambda_1} \frac{J_m(\lambda_1 \omega h)}{J'_m(\lambda_1 \omega h)} \right.
$$
$$
\left. - \frac{(1 - sM_2)^2}{\lambda_2} \frac{J_m(\lambda_2 \omega h)H_m^{(1)'}(\lambda_2 \omega) - H_m^{(1)}(\lambda_2 \omega h)J'_m(\lambda_2 \omega)}{J'_m(\lambda_2 \omega h)H_m^{(1)'}(\lambda_2 \omega) - H_m^{(1)'}(\lambda_2 \omega h)J'_m(\lambda_2 \omega)} \right\}.
\tag{4.10}
$$

It is clear from (4.9) that s_o appears as a simple pole in (4.7), so the scattered instability potential is easily obtained simply via its residue,

$$
\psi_s(r, z) = \omega \exp(\mathrm{i}\omega s_o z) \lim_{s \to s_o} [\hat{\beta}^+(s)]
$$
$$
\times H(z) \begin{cases} (1 - s_o M_1) \lim_{s \to s_o} [Y_1(r, s)/\lambda_1] & \text{for} \quad r < h, \\ (1 - s_o M_2) \lim_{s \to s_o} [Y_2(r, s)/\lambda_2] & \text{for} \quad h < r < 1, \end{cases} \quad (4.11)
$$

to yield the incident instability wave for the full problem. Comparing (4.11) with (2.14), it is easy to see that

$$
B_{mn}^+ = \omega \exp(-\mathrm{i}\omega s_p z_o) \lim_{s \to s_p} [\hat{\beta}^+(s)], \quad (4.12)
$$

and the mode shape is

$$
\Psi_{mn}(r) = H(z - z_o) \begin{cases} (1 - s_p M_1) \lim_{s \to s_p} [Y_1(r, s)/\lambda_1] & \text{for} \quad r < h, \\ (1 - s_p M_2) \lim_{s \to s_p} [Y_2(r, s)/\lambda_2] & \text{for} \quad h < r < 1, \end{cases} \quad (4.13)
$$

with $\mu_{mn}^+ = s_o = s_p$. The factor $\exp(-\mathrm{i}\omega s_p z_o)$ appears in (4.12) since the vortex sheet originates at z_o. Unlike in §3.3 we are not concerned with the scattered acoustic field here and thus the full solution of this auxiliary problem is unnecessary.

5. Near-field solutions

The numerical methods to accurately evaluate (3.35) are summarized in the Appendix. In this section, we present the near-field solutions for pressure for incident acoustic and vorticity waves. These solutions support exponentially growing instability waves, which are of course not physically realizable. However, the utility of the model depends primarily upon how well the shape and dispersion characteristics of the instability waves represent the pressure fields associated with the turbulence structures at the shroud exit. This near-field pressure similarity has recently been confirmed by matching the predicted near fields of instability waves with the near-field pressure of turbulence structures in a high-Reynolds-number jet (Suzuki & Colonius 2006). In addition, studies on large coherent structures in turbulent shear flows (e.g. Strange & Crighton 1983; Gaster, Kit & Wygnanski 1985) have shown that linear theory can accurately predict the local transverse mode shapes and phase characteristics of instabilities along with their dispersion relations, even for strong nonlinear disturbances. These aspects have also been discussed in detail by Crighton (1992) in the context of linear models such as the present. Amplitude predictions would, of course, require additional procedures which are beyond the scope of the current theoretical study and would probably involve large-scale simulations.

5.1. *Incident acoustic wave*

For an example solution, we choose $h = 0.65$, $M_1 = 0.9$, $M_2 = 0.25$, $M_3 = 0.1$, and $\omega = 4.5$ with the azimuthal mode number $m = 1$. For these input parameters there is only one right-propagating acoustic mode ($n = 1$). Figure 8(a) shows the incident acoustic wave and figure 8(b) shows the entire near-field acoustic component of pressure. The reflected waves moving leftward inside the shroud and part of the scattered wave field are shown in figure 8(c). Figures 8(d) and 8(e) show the instability waves excited on the inner and outer vortex sheets, respectively. The outer vortex sheet is perturbed with shorter wavelengths, as expected for the selected flow Mach
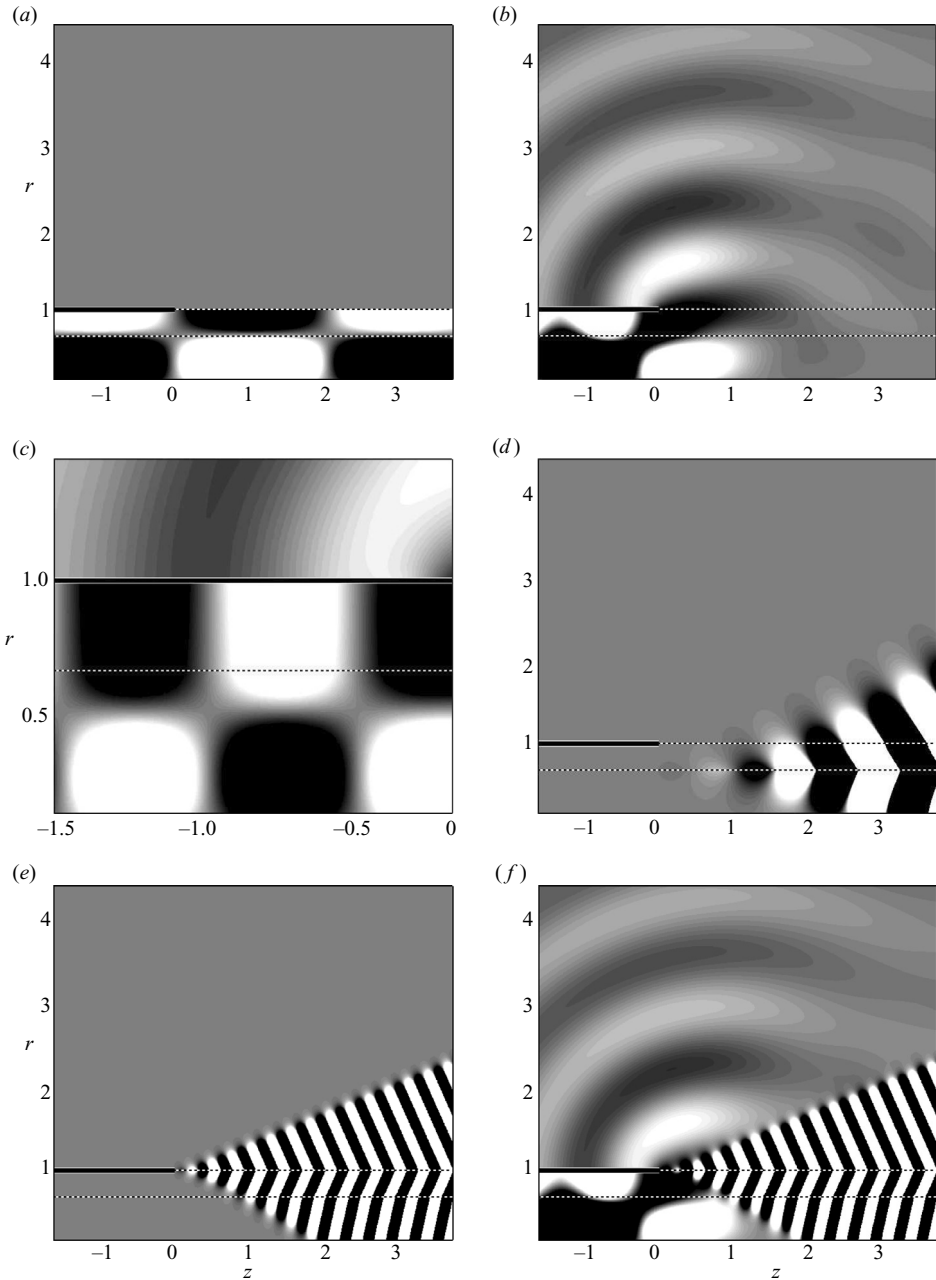
FIGURE 8. Real part of the pressure for the incident acoustic mode $(1, 1)$: (*a*) the incident wave; (*b*) the acoustic part of the pressure field; (*c*) the scattered and reflected acoustic pressure waves; (*d*) the instability wave of the inner shear layer; (*e*) the instability wave of the outer shear layer; and (*f*) the total pressure field. Grey levels indicate pressure between ± 0.4 for an incident wave with unit amplitude.

numbers. The vorticity wave on the outer sheet is also of higher amplitude, which can be seen in figure 8(*f*), which shows the complete solution. The outer wave is expected to be of much higher amplitude since it is seeded at a sharp edge, and thus should be more receptive than the inner. For example, at $z = 2$, the outer wave has an amplitude

almost 10^8 higher than the inner. The instability waves grow exponentially in z but decay exponentially in the r-direction yielding the wedge shapes for the influence of the vorticity waves.

5.2. *Incident vorticity wave*

For this demonstration, we retain the same flow parameters as in the previous section for the acoustic wave. Figure 9(a) shows the incident vorticity wave that originates from the assumed inner nozzle lip at $z_o = -1.5$. Figure 9(b) shows the scattered acoustic field generated by the incident instability wave together with the ($r > 1, z > 0$) portion of this instability wave which, unlike in the preceding subsection, is computed in conjunction with the scattered acoustic field (see the Appendix, §A.1). Most of the energy of the incident vorticity wave transmits, but a portion is scattered into acoustic waves that seem to radiate outwards from the shroud edge and reflect back inside of the shroud (figure 9c). Figure 9(d) shows the pressure associated with the outer vortex sheet instability and figure 9(e) shows the total pressure field, a superposition of the components shown in figures 9(b) and 9(d). The vorticity waves in $z > 0$ are of more comparable magnitude in this case. At $z = 2$ the outer wave amplitude is about 10^4 higher than the inner.

Figure 10 shows the field generated when there is no propagating reflected mode. The parameters are selected with reference to figure 14(a) so that the data point lies in the 'no reflection' zone. The non-propagating reflected waves are seen to decay over a very short upstream distance in figure 10(c). Figure 10(f) shows the plot of the kernel poles and zeros for this case. As expected, there is no pole lying on the real axis in between the left branch cut and the (Γ) contour crossover point, which is where the propagating reflected modes are found. In any such situation a pole is always present between the branch points s_1^- and s_2^-, as can be seen in figure 10(f), but it lies on the left branch cut. With changing parameters, this pole can move along the real axis. As it leaves the left branch cut it becomes a valid propagating reflecting mode for the system. However, for a given set of parameters, there might be multiple such poles with some of them as propagating modes and the rest lying on the cut (e.g. figure 4b).

6. Shroud-exit reflectivity

In this section we consider the acoustic wave reflected by the shroud exit, which potentially closes a resonance loop as discussed in §1.1.

6.1. *Reflectivity formulation*

Reflection coefficients for both acoustic and vortical incident waves can be defined using the same framework. For each pair of incident and reflected modes we first consider the modal decomposition of the pressure field inside the shroud:

$$p(r, z) = \sum_{m=-\infty}^{\infty} \sum_{n=1}^{\infty} [A_{mn}^+ \exp(\mathrm{i}\mu_{mn}^+ \omega z) + A_{mn}^- \exp(\mathrm{i}\mu_{mn}^- \omega z)] \Psi_{mn}(r), \qquad (6.1)$$

which is analogous to (2.10) for the velocity potential. Here $A_{mn}^\pm$ are the right- ($+$) and left- ($-$) propagating pressure wave amplitudes. The reflection coefficient for the (m, l) mode reflection of an incident (m, n) mode is defined as

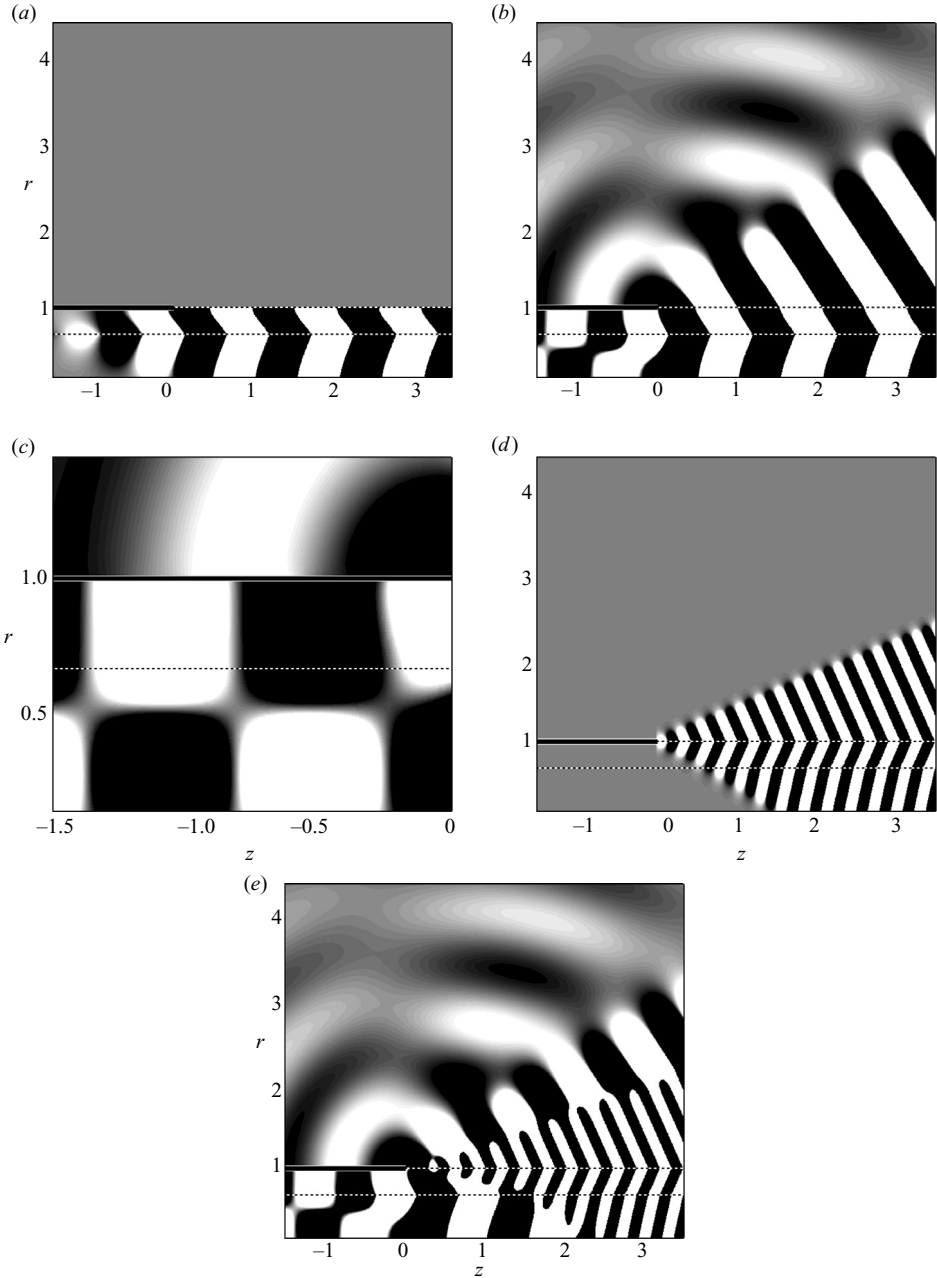$$R_{mnl} = \frac{A_{ml}^-}{A_{mn}^+}. \qquad (6.2)$$

FIGURE 9. Real part of the pressure for the incident instability mode for $h = 0.65$, $M_1 = 0.09$, $M_2 = 0.25$, $M_3 = 0.1$, $\omega = 4.5$, $m = 1$: (*a*) the incident wave; (*b*) the acoustic part of the pressure field and inner instability wave superimposed; (*c*) the scattered and reflected acoustic pressure waves; (*d*) the instability wave of the outer shear layer; and (*e*) the total pressure field. Grey levels indicate pressure between ± 0.4. The seed acoustic wave (see §4.2) has unity amplitude.

The incident wave amplitude A_{mn}^+ is straightforward to identify. By applying (3.34) to (2.14), we can write the pressure field inside the shroud as

$$p_i(r, z) = \begin{cases} i\omega(1 - \mu_{mn}^+ M_1) B_{mn}^+ \Psi_{mn}(r) \exp(i\omega\mu_{mn}^+ z) & \text{for} \quad r < h, \\ i\omega(1 - \mu_{mn}^+ M_2) B_{mn}^+ \Psi_{mn}(r) \exp(i\omega\mu_{mn}^+ z) & \text{for} \quad h < r < 1. \end{cases} \quad (6.3)$$
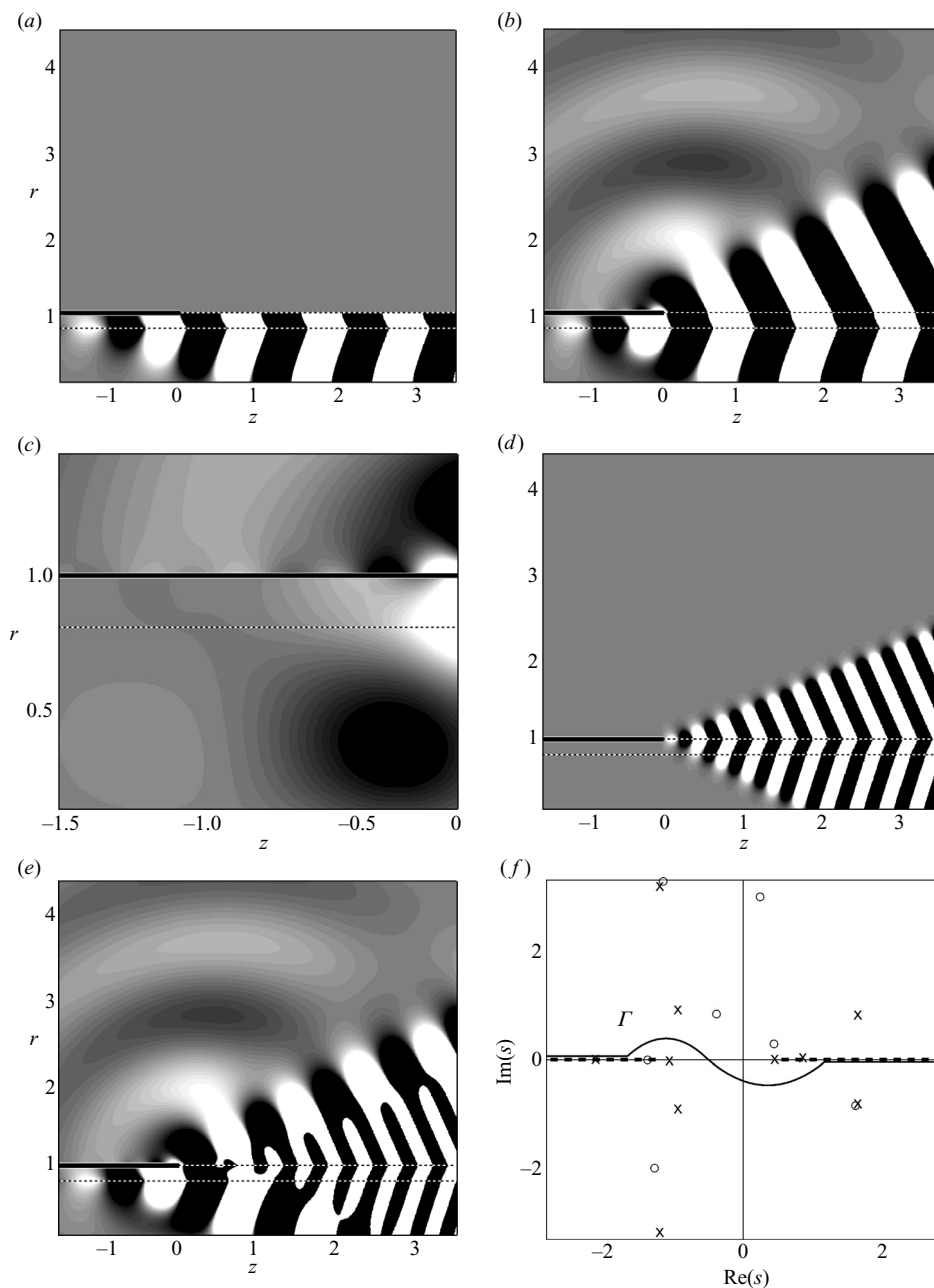
FIGURE 10. (a–e) Same as figure 9 for $M_1 = 0.7$, $M_2 = 0.25$, $M_3 = 0.1$, $h = 0.8$, $\omega = 3.5$, and $m = 1$. (f) Location of the zeros ($\circ$) and poles ($\times$) of $K(s)$ in (3.22) as $\delta \to 0$.

Comparing (6.3) to (6.1) we see that the amplitude of the incident wave is thus

$$A_{mn}^+ = \begin{cases} \mathrm{i}\omega B_{mn}^+ (1 - \mu_{mn}^+ M_1) & \text{for} \quad r < h, \\ \mathrm{i}\omega B_{mn}^+ (1 - \mu_{mn}^+ M_2) & \text{for} \quad h < r < 1. \end{cases} \tag{6.4}$$

For incident acoustic waves we take $B_{mn}^+ = 1$, while for incident vorticity waves it is given by (4.12). Consequently, for incident instability waves A_{mn}^+ is the pressure amplitude at the shroud exit.

Computing the pressure amplitude A_{ml}^- of the reflected mode is more involved. The net scattered pressure is the sum of the acoustic and instability parts as given by (3.35) and (3.37), respectively. The contour integral in (3.35) can be evaluated for individual wave components of the full solution using the residue theorem. Since we seek amplitudes of the modes inside the shroud ($r < 1, z < 0$), only the poles lying below Γ in the lower-half-plane (R^+) are needed. This is because the transformed fields, as defined, are analytic in R^- for $z < 0$. So, the poles corresponding to the waves inside the shroud ($z < 0$) must only lie in R^+. In order to be non-decaying they must also lie on the real axis between the left and right branch cuts (see figure 3b). Reflectivities are only well-defined for these propagating reflected modes (m, l), so to compute them the field inside the shroud can be written via the residue theorem as

$$p(r, z) = -\mathrm{i}\omega^2 \sum_{l=1}^{\infty} \sum_{m=-\infty}^{\infty} \exp(\mathrm{i}\omega\mu_{ml}^- z)\,(1 - \mu_{ml}^- M_2)^2$$

$$\times \lim_{s \to \mu_{ml}^-} [\hat{\xi}^+(s)] \begin{cases} \lim_{s \to \mu_{ml}^-}(T_1(r, s)/\lambda_2) & \text{for} \quad r < h, \\ \lim_{s \to \mu_{ml}^-}(T_2(r, s)/\lambda_2) & \text{for} \quad h < r < 1. \end{cases} \quad (6.5)$$

The next task is to write both cases of (6.5) in a form similar to (6.1) to identify A_{ml}^-. The shapes of the reflected modes inside the shroud are the same as the incident acoustic modes given by (4.1), but for a wavenumber of μ_{ml}^-, and therefore are already known. To evaluate the limits in (6.5) we start with (3.5), where we can solve $\lambda_p^2 = (1 - sM_p)^2 - s^2$ for s as

$$s = \frac{-M_p \pm \sqrt{1 - (1 - M_p^2)\lambda_p^2}}{1 - M_p^2} \quad \text{for} \quad p = 1, 2. \quad (6.6)$$

Likewise, from (4.2) it can be shown that

$$\mu_{ml}^- = \frac{-M_1 - \sqrt{1 - (1 - M_1^2)\alpha_{ml}^2/\omega^2}}{1 - M_1^2} = \frac{-M_2 - \sqrt{1 - (1 - M_2^2)\beta_{ml}^2/\omega^2}}{1 - M_2^2}. \quad (6.7)$$

Together, these indicate that as $s \to \mu_{ml}^-$

$$\lambda_1 \to \alpha_{ml}/\omega \quad \text{and} \quad \lambda_2 \to \beta_{ml}/\omega. \quad (6.8)$$

To explicitly evaluate the factors involving T_1 in (6.5) for the $r < h$ case we start with its definition (3.33a), substitute $R(s)$ from (3.19) and employ (4.3). Then taking the limit as $s \to \mu_{ml}^-$ yields

$$\lim_{s \to \mu_{ml}^-} T_1(r, s) = \beta_{ml}(1 - \mu_{ml}^- M_1)^2 \Psi_{ml}(r) \frac{\mathrm{J}_m'(\beta_{ml}h)\mathrm{H}_m^{(1)}(\beta_{ml}h) - \mathrm{H}_m^{(1)\prime}(\beta_{ml}h)\mathrm{J}_m(\beta_{ml}h)}{\Lambda'(\mu_{ml}^-)}, \quad (6.9)$$

where we have also used (4.1) for $r < h$ and (6.8). Substituting (6.9) in (6.5) yields

$$p(r, z) = -\mathrm{i}\omega^3 \sum_{l=1}^{\infty} \sum_{m=-\infty}^{\infty} \exp(\mathrm{i}\omega\mu_{ml}^- z)(1 - \mu_{ml}^- M_1)^2(1 - \mu_{ml}^- M_2)^2\hat{\xi}^+(\mu_{ml}^-)$$

$$\times \frac{\mathrm{J}_m'(\beta_{ml}h)\mathrm{H}_m^{(1)}(\beta_{ml}h) - \mathrm{H}_m^{(1)\prime}(\beta_{ml}h)\mathrm{J}_m(\beta_{ml}h)}{\Lambda'(\mu_{ml}^-)}\Psi_{ml}(r). \quad (6.10)$$

Comparing this with (6.1) shows that

$$
A_{ml}^- = -i\omega^3 \frac{(1 - \mu_{ml}^- M_1)^2 (1 - \mu_{ml}^- M_2)^2 \hat{\xi}^+(\mu_{ml}^-)}{\Lambda'(\mu_{ml}^-)}
$$

$$
\times [J_m'(\beta_{ml}h) H_m^{(1)}(\beta_{ml}h) - H_m^{(1)\prime}(\beta_{ml}h) J_m(\beta_{ml}h)] \quad \text{for} \quad r < h. \quad (6.11)
$$

Similarly, for $r > h$ we start by substituting (3.19) into (3.33b). Then we apply the limit

$$
\lim_{s \to \mu_{ml}^-} \left[\lambda(s) \frac{H_m^{(1)\prime}(\lambda_2 \omega h)}{H_m^{(1)\prime}(\lambda_2 \omega)} J_m(\lambda_1 \omega h) - \frac{H_m^{(1)}(\lambda_2 \omega h)}{H_m^{(1)\prime}(\lambda_2 \omega)} J_m'(\lambda_1 \omega h) \right]
$$

$$
= \lambda(s) \frac{J_m'(\lambda_2 \omega h)}{J_m'(\lambda_2 \omega)} J_m(\lambda_1 \omega h) - \frac{J_m(\lambda_2 \omega h)}{J_m'(\lambda_2 \omega)} J_m'(\lambda_1 \omega h), \quad (6.12)
$$

which is obtained from $\Lambda(s) \to 0$ (see (4.3)) as $s \to \mu_{ml}^-$. Additional algebraic manipulations lead to

$$
\lim_{s \to \mu_{ml}^-} T_2(r, s) = \alpha_{ml} \frac{(1 - \mu_{ml}^- M_2)^3}{(1 - \mu_{ml}^- M_1)} \frac{\Psi_{ml}(r)}{\Lambda'(\mu_{ml}^-)} \frac{J_m'(\beta_{ml}) H_m^{(1)}(\beta_{ml}h) - H_m^{(1)\prime}(\beta_{ml}) J_m(\beta_{ml}h)}{J_m(\alpha_{ml}h)}
$$

$$
\times \frac{\lambda(\mu_{ml}^-) H_m^{(1)\prime}(\beta_{ml}h) J_m(\alpha_{ml}h) - J_m'(\alpha_{ml}h) H_m^{(1)}(\beta_{ml}h)}{H_m^{(1)\prime}(\beta_{ml})}. \quad (6.13)
$$

Substituting (6.13) in (6.5) yields the pressure for the $r > h$ case,

$$
p(r, z) = -i\omega^3 \sum_{l=1}^{\infty} \sum_{m=-\infty}^{\infty} \exp(i\omega \mu_{ml}^- z) \frac{(1 - \mu_{ml}^- M_1)(1 - \mu_{ml}^- M_2)^3}{\Lambda'(\mu_{ml}^-) \lambda(\mu_{ml}^-)} \hat{\xi}^+(\mu_{ml}^-)
$$

$$
\times \frac{J_m'(\beta_{ml}) H_m^{(1)}(\beta_{ml}h) - H_m^{(1)\prime}(\beta_{ml}) J_m(\beta_{ml}h)}{J_m(\alpha_{ml}h)}
$$

$$
\times \frac{\lambda(\mu_{ml}^-) H_m^{(1)\prime}(\beta_{ml}h) J_m(\alpha_{ml}h) - J_m'(\alpha_{ml}h) H_m^{(1)}(\beta_{ml}h)}{H_m^{(1)\prime}(\beta_{ml})} \Psi_{ml}(r), \quad (6.14)
$$

which upon comparison with (6.1) gives

$$
A_{ml}^- = -i\omega^3 \frac{(1 - \mu_{ml}^- M_1)(1 - \mu_{ml}^- M_2)^3}{\Lambda'(\mu_{ml}^-) \lambda(\mu_{ml}^-)} \hat{\xi}^+(\mu_{ml}^-) \frac{J_m'(\beta_{ml}) H_m^{(1)}(\beta_{ml}h) - H_m^{(1)\prime}(\beta_{ml}) J_m(\beta_{ml}h)}{J_m(\alpha_{ml}h)}
$$

$$
\times \frac{\lambda(\mu_{ml}^-) H_m^{(1)\prime}(\beta_{ml}h) J_m(\alpha_{ml}h) - J_m'(\alpha_{ml}h) H_m^{(1)}(\beta_{ml}h)}{H_m^{(1)\prime}(\beta_{ml})} \quad \text{for} \quad r > h. \quad (6.15)
$$

Finally, substituting (6.4), (6.11) and (6.15) into (6.2) yields the reflective coefficients:

$$R_{mnl} = \begin{cases} \left| \omega^2 \dfrac{(1 - \mu_{ml}^- M_1)^2 (1 - \mu_{ml}^- M_2)^2 \hat{\xi}^+(\mu_{ml}^-)}{B_{mn}^+ (1 - \mu_{mn}^+ M_1) \Lambda'(\mu_{ml}^-)} \right. \\ \qquad \times \left. [\mathrm{J}'_m(\beta_{ml} h) \mathrm{H}_m^{(1)}(\beta_{ml} h) - \mathrm{H}_m^{(1)\prime}(\beta_{ml} h) \mathrm{J}_m(\beta_{ml} h)] \right| \qquad \text{for} \quad 0 < r < h, \\[12pt] \left| \omega^2 \dfrac{(1 - \mu_{ml}^- M_1)(1 - \mu_{ml}^- M_2)^3 \hat{\xi}^+(\mu_{ml}^-)}{B_{mn}^+ (1 - \mu_{mn}^+ M_2) \Lambda'(\mu_{ml}^-) \lambda(\mu_{ml}^-)} \right. \\ \qquad \times \left[\dfrac{\lambda(\mu_{ml}^-) \mathrm{H}_m^{(1)\prime}(\beta_{ml} h) \mathrm{J}_m(\alpha_{ml} h) - \mathrm{J}'_m(\alpha_{ml} h) \mathrm{H}_m^{(1)}(\beta_{ml} h)}{\mathrm{H}_m^{(1)\prime}(\beta_{ml})} \right] \\ \qquad \times \left. \left[\dfrac{\mathrm{J}'_m(\beta_{ml}) \mathrm{H}_m^{(1)}(\beta_{ml} h) - \mathrm{H}_m^{(1)\prime}(\beta_{ml} h) \mathrm{J}_m(\beta_{ml} h)}{\mathrm{J}_m(\alpha_{ml} h)} \right] \right| \qquad \text{for} \quad h < r < 1, \end{cases}$$

$$(6.16)$$

where $\hat{\xi}^+(\mu_{ml}^-)$ is obtained from the final stage of the Wiener–Hopf solution in (3.30).

6.2. *Reflectivity results*

The computational methods for computing reflectivities are summarized in the Appendix, §A.3. In this section we consider results for specific incident waves.

6.2.1. *Incident acoustic wave*

One interesting aspect of the reflectivities is that the shroud exit is non-reflecting – completely 'transparent' – for certain parameters. Consider for example, the reflectivities plotted in figure 11. For this case, only modes with $m \leqslant 3$ fall into the frequency range $0 < \omega < 5$ plotted. For any m there is only one radial mode that is right propagating, so only three incident modes $(1, 1)$, $(2, 1)$ and $(3, 1)$ are considered. For each m, only reflected mode $(m, l) = (m, 1)$ propagates, so there are only three reflection coefficients R_{111}, R_{211} and R_{311}. These are plotted in figure 11, separately for $r < h$ and $h < r < 1$. These reflectivities are undefined over finite ranges of frequencies for which there is no propagating reflected wave unlike, for example, the single-jet reflectivity curves of Munt (1990). In these regions only decaying reflected modes are available, for which reflection coefficients are undefined. It is the discontinuity in the mean flow inside the shroud that significantly reduces the number of propagating modes, leading to these regions for which the shroud exit is effectively transparent. These non-reflecting zones reduce for smaller h as can be seen in figure 12. For undefined $R_{mnl}(\omega)$, either the corresponding incident or reflected mode is non-propagating, or both. The reflectivities generally decrease with ω, though not always monotonically (figure 11). The higher-order azimuthal modes (larger m) generally have lower reflectivities, as expected. Also the reflectivities here are higher in the core jet than in the co-flow, though this depends on the parameters chosen. This is important for the jet resonance problem discussed in §1 because it provides an estimate of how much acoustic energy leaks, and therefore must be replenished by coupling with the jet.

6.2.2. *Incident vorticity wave*

One of our main concerns is how much of the instability wave energy is reflected into acoustic modes. The reflection coefficients of the incident vorticity waves for different m, reflected back into the $(1, 1)$ acoustic mode inside the shroud, are shown in figure 13 for $0 < \omega < 5$. We denote the incident instability modes as (m, v), where v stands for vorticity. Conversion of incident vorticity modes into reflected propagating
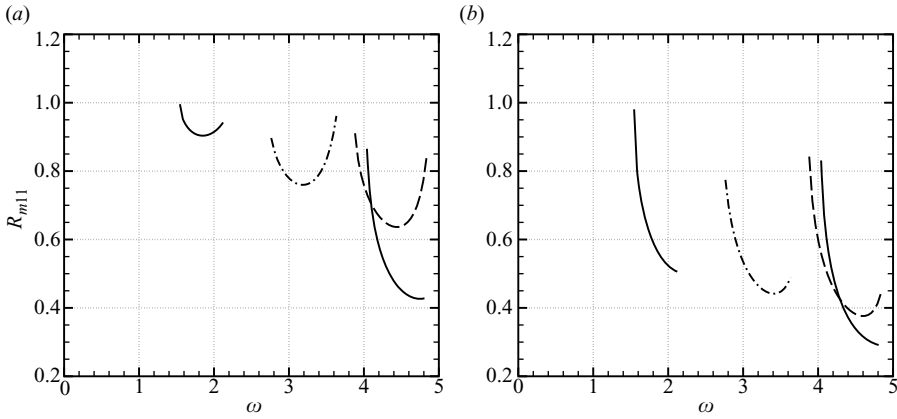
(a)

(b)

FIGURE 11. The reflection coefficients, R_{mnl} for various propagating incident acoustic modes: ——, R_{111}; —·—, R_{211}; — —, R_{311} for (a) $r < h$ and (b) $r > h$. Parameters are $M_1 = 0.9$, $M_2 = 0.25$, $M_3 = 0.1$, and $h = 0.65$.
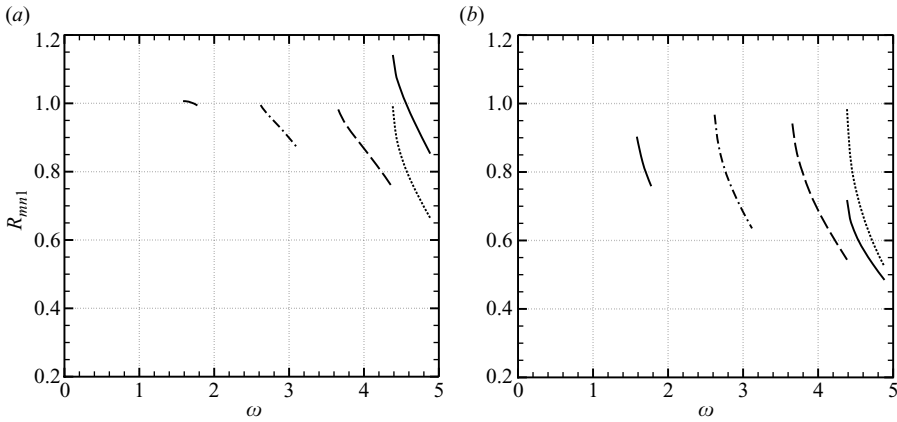
(a)

(b)

FIGURE 12. Same as figure 11 but for $M_1 = 0.6$, $M_2 = 0.25$, $M_3 = 0.1$, and $h = 0.9$. In addition $\ldots$, R_{121}.
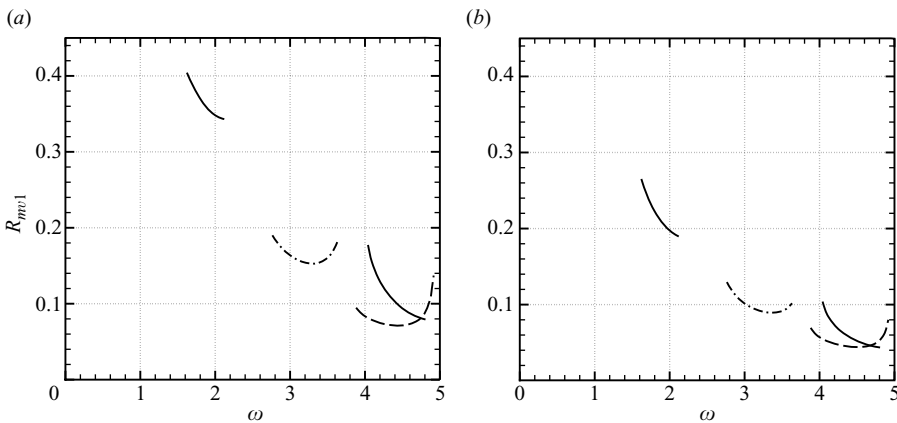
(a)

(b)

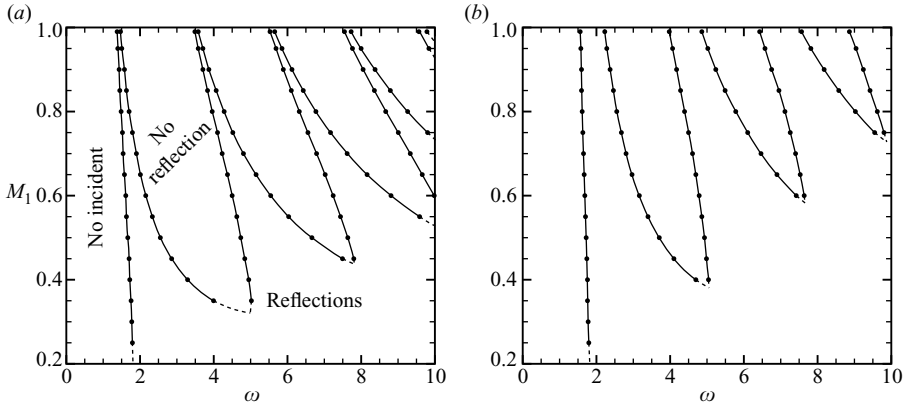FIGURE 13. Same parameters as in figure 11, but for incident instability modes (m, v).

FIGURE 14. Zones of finite and zero reflectivity for $M_2 = 0.25$, $M_3 = 0.1$, and $m = 1$:
(*a*) $h = 0.8$; (*b*) $h = 0.6$. Dashed lines show extrapolations.

acoustic modes is more restrictive and thus the frequency ranges for finite reflectivities is narrower here than for incident acoustic modes (although this is not apparent in figure 13). Also, note that these reflectivities are smaller than the acoustic mode reflectivities. Of course, since in realistic flows the pressures associated with vortical structures are many times greater than acoustic pressures, these small reflectivities are still potentially important.

To provide a clearer picture of the circumstances under which the shroud exit is transparent to outgoing instabilities, we plot the boundary of this behaviour in an M_1–ω plane for two cases in figure 14. The intermittent character of the boundary shown in these plots might explain the experimental observations, such as of Bradshaw *et al.* (1968), who report strong subsonic shrouded resonances for multiple ranges of jet Mach numbers under otherwise similar flow conditions. The complex structure of the reflecting/non-reflecting boundary is set by whether or not a particular propagating reflected acoustic mode exists, which in turn is governed by the dispersion relation (4.3). The Bessel functions in (4.3) yield the quasi-periodic behaviour seen in figure 14. For $M_1 = M_2$, there is always a reflecting mode, so we expect the region of finite reflectivity to broaden as $M_1 \to M_2$. This is seen in the figure. We can also anticipate the trend toward more reflection possibilities for higher ω. For $\omega \to 0$, only plane waves are possible, which cannot exist across multiple streams. The matching condition between streams is more easily satisfied for higher frequencies, and for $\omega \to \infty$ there is no effective restriction on the reflected modes. Note that the no-incident cutoffs are dictated by the requirement that the acoustic wave used to seed the incident vorticity wave be propagating inside the (virtual) nozzle (see text after (4.9) for the cutoff expression). In actual situations the vorticity wave may be reinforced by acoustic modes from elsewhere or by the non-propagating evanescent modes for short shrouds. Thus there may be potential resonance situations for frequencies below this cutoff.

6.2.3. *Effect of suppressing vortex shedding at the shroud exit*

It has been suggested that finite-thickness shear layers might not satisfy the full Kutta condition at higher Strouhal numbers (e.g. Bechert & Pfizenmaier 1975). We can make an assessment of the specific effect of the Kutta condition in our model by suppressing the vortex shedding. This is achieved by setting $\gamma = 0$ in (3.31) which cancels the term $(s - s_{z_2})$ in (3.31), suppressing any vortex shedding by the
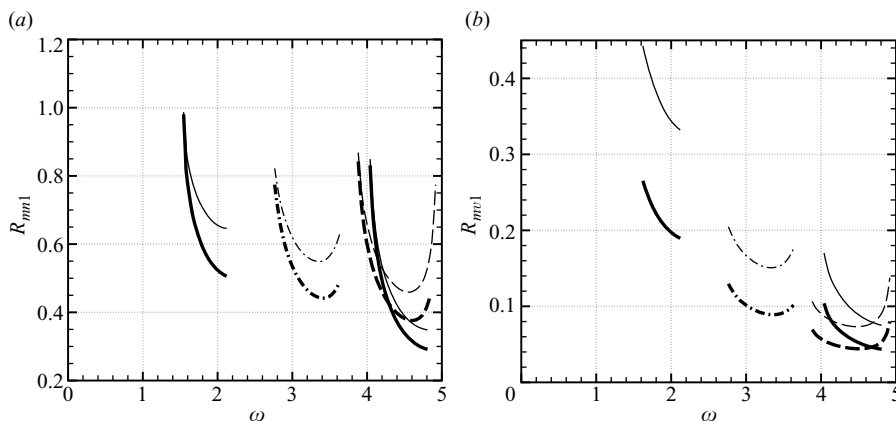
FIGURE 15. Effect of the Kutta condition on reflectivity for $r > h$: (*a*) incident acoustic modes and (*b*) incident vorticity modes with the full Kutta condition $\gamma = 1$ (thick lines) and suppressed vortex shedding $\gamma = 0$ (thin lines). Other parameters are same as in figures 11 and 13.

outer vortex sheet. Figure 15 compares the no-vorticity solutions with the full Kutta condition solutions obtained previously. Suppressing vortex shedding is known to increase radiation to the far field (Gabard & Astley 2006; Demir & Rienstra 2007). Here it is seen to increase reflectivities. The other interesting aspect of note here is that for incident acoustic modes reducing $|\gamma|$ has more effect on reflectivities for higher ω, unlike acoustic radiation which is affected more at lower frequencies (Rienstra 1983). In contrast, incident vorticity mode reflectivities seem to be more affected at lower ω.

7. Conclusions

The main result of this study is the reflectivity of vorticity waves back into the shroud as acoustic modes. These reflectivities are lower than the corresponding reflectivities of outgoing acoustic modes, but the vorticity waves would be expected to contain many times more energy in a turbulent jet, so these small reflectivities are potentially important. The most notable aspect of these reflectivities are the bands in M_1–ω coordinates for which there is no reflection. This switch over between reflecting and transparent behaviour of the shroud exit might explain the sensitivities of observed howling resonances to Mach numbers (Bradshaw *et al.* 1968). For jet diameters larger than about half the shroud diameter, these transparent conditions seem to become prevalent.

The analysis here provides an indication of when a strong feedback loop might exist inside the shroud which, however, does not necessarily mean resonance. An obvious extension of this study would be to couple the nozzle of the auxiliary problem of § 4.2 with the shroud exit analysis and seek to find resonance conditions. The nozzle, although used to seed the vorticity wave, has not been considered further in the analysis. The reflected acoustic modes travel upstream and should undergo the mode conversion of acoustic to vortical at the nozzle lip at the given frequency. It would also be of interest to consider extension to supersonic flow conditions for which resonances are also observed.

Appendix. Numerical procedures

A.1. *Kernel split functions and contour integrals*

The kernel (3.22) appears to defy explicit factorization, so $\tilde{K}^+(s)$ is evaluated using the general factorization formula (e.g. Noble 1988):

$$\log \tilde{K}^+(s) = -\frac{1}{2\pi i} \int_C \frac{\log[K(\sigma)/U(\sigma)]}{\sigma - s} \, d\sigma, \qquad (A\,1)$$

where C is the integration path from $-\infty + 0i$ to $\infty - 0i$ in S, similar but distinct from Γ. C must lie above Γ. $\tilde{K}^-(s)$ is then obtained from (3.23). The factor $U(\sigma)$ in (A 1) is from (3.24) and thus removes the instability zeros and pole for the incident acoustic case, so C does not need to be deformed to account for them. For the incident vorticity case, however, for reasons discussed in §3.3, $U(\sigma)$ is given by (3.25). In this case, C must be deformed around both s_{z_1} and s_p. The point where C crosses the real axis has to be carefully chosen to preserve analytic continuity (see the discussion after (3.30)). Also, a large number of acoustic zeros and poles lie on the real axis near the origin of the complex plane where the kernel integration is done. This would put severe demands upon the adaptive quadrature routines were C to pass near to them, so C is deformed in the same way as Γ in figure 4(*b*). The limits for the kernel integrals are taken such that the contribution of the integrand becomes negligible beyond the limits. An adaptive quadrature scheme using the trapezoidal rule has been used to compute the kernel integrals. It was also confirmed that $\tilde{K}(s) = K(s)/U(s)$ in (A 1) does not cross the negative real axis on C, which is a condition that must be satisfied (see Rienstra 2007).

The inverse transform integrals over Γ are only computed for near-field solutions of §5. Apart from Γ being similar to C, but lying below, the inversion integrations need to be computed over much smaller limits since the inversion integrand contribution falls much faster with increasing $|s|$ along Γ. The kernel integrations need to be computed only once and then the inversion integrals may be computed for any (r, z) pair (see (3.32), (3.35)). It is less computationally expensive here to compute the inversion integrals at a fixed set of points without adaptive refinement and, accordingly, a simple quadrature scheme is used to compute it.

A.2. *Kernel approximations*

The special functions are computed using standard routines but extra care is needed for certain ranges of arguments. Computation of (3.22), for example, requires special consideration of two factors:

$$K_1 = \frac{H_m^{(1)}(\lambda_2 \omega) + R(s) J_m(\lambda_2 \omega)}{H_m^{(1)\prime}(\lambda_2 \omega) + R(s) J_m^\prime(\lambda_2 \omega)} \quad \text{and} \quad K_2 = \frac{H_m^{(1)}(\lambda_3 \omega)}{H_m^{(1)\prime}(\lambda_3 \omega)}. \qquad (A\,2)$$

For arguments z with large imaginary part, Bessel functions behave like $\exp(|\text{Im}(z)|)$, while the Hankel functions behave as $\exp(iz)$. The primary requirement is to use scaled functions which compensate for these behaviours. However, for very large arguments, when the round-off errors of the denominators of (A 2) become significant, the asymptotic forms for large $|\lambda_p \omega|$, $p = 1, 2, 3$,

$$K_1 \approx i \quad \text{and} \quad K_2 \approx \frac{8\lambda_3 \omega + 4im^2 - i}{8i\lambda_3 \omega - 4m^2 - 3}, \qquad (A\,3)$$

are used.

A.3. *Reflectivity computations*

Computations of reflectivity coefficients using (6.16) are relatively straightforward and less expensive, since as in the §5 computations no inverse transform is necessary. The kernel integrals, however, appear in the determination of $\hat{\xi}^+(\mu_{ml}^-)$ (see (3.30)), where the split kernels $\hat{K}^-(\mu_{mn}^+)$ and $\hat{K}^+(\mu_{ml}^-)$ need to be found using the procedures of §A.1, but only at μ_{mn}^+ and μ_{ml}^+, respectively. This allows reflectivities to be computed over ranges of ω as presented in §6.2 with relatively little computation time.

REFERENCES

BECHERT, D. & PFIZENMAIER, E. 1975 Optical compensation measurements on the unsteady exit condition at a nozzle discharge edge. *J. Fluid Mech.* **71**, 123–144.

BRADSHAW, P., FLINTOFF, J. L. & MIDDLETON, D. 1968 Unexplained scale effects in ejector shroud "howling". *J. Sound Vib.* **7**, 183–190.

CARRIER, G. 1956 Sound transmission from a tube with flow. *Q. Appl. Maths* **13**, 457–461.

CRIGHTON, D. G. 1972a Radiation properties of the semi-infinite vortex sheet. *Proc. R. Soc. Lond.* A **330**, 185–198.

CRIGHTON, D. G. 1972b The excess noise fields of subsonic jets. *J. Fluid Mech.* **56**, 683–694.

CRIGHTON, D. G. 1992 The jet edge-tone feedback cycle; linear theory for the operating stages. *J. Fluid Mech.* **234**, 361–391.

CRIGHTON, D. G. & LEPPINGTON, F. G. 1974 Radiation properties of the semi-infinite vortex sheet: The initial-value problem. *J. Fluid Mech.* **64**, 393–414.

CROW, S. C. & CHAMPAGNE, F. H. 1971 Orderly structure in jet turbulence. *J. Fluid Mech.* **48**, 547–591.

DEMIR, A. & RIENSTRA, S. W. 2007 Sound radiation from a buried nozzle with jet and bypass flow. *ICSV14 Paper* 449. Cairns.

GABARD, G. & ASTLEY, R. J. 2006 Theoretical model for sound radiation from annular jet pipes: far- and near-field solutions. *J. Fluid Mech.* **549**, 315–341.

GASTER, M., KIT, E. & WYGNANSKI, I. 1985 Large-scale structures in a forced turbulent mixing layer. *J. Fluid Mech.* **150**, 23–39.

HEATON, C. J. & PEAKE, N. 2005 Acoustic scattering in a duct with mean swirling flow. *J. Fluid Mech.* **540**, 189–220.

HOMICZ, G. F. & LORDI, J. A. 1975 A note on the radiative directivity patterns of duct acoustic modes. *J. Sound Vib.* **41**, 283–290.

HOWE, M. S. 1979 Attenuation of sound in a low Mach number nozzle flow. *J. Fluid Mech.* **91**, 209–229.

HOWE, M. S. 1987 Self-excited oscillation in jet engine test cells. *J. Fluids Struct.* **1**, 121–148.

JONES, D. S. & MORGAN, J. D. 1974 A linear model of a finite amplitude Helmholtz instability. *Proc. R. Soc. Lond* A **338**, 17–41.

JONES, R. R. III & LAZALIER, G. R. 1992 The acoustic response of altitude test facility exhaust systems to axisymmetric and two-dimensional turbine engine exhaust plumes. In *DGLR/AIAA 14th Aeroacoustics Conference, Eurogress Center, Auchen, Germany*, *DGLR-Bericht 92-03*, vol. II.

LEE, B. H. K. & JONES, D. J. 1973 Transmission of upstream sound through a subsonic jet. *AIAA Paper* 73-630.

LEVINE, H. & SCHWINGER, J. 1948 On the radiation of sound from an unflanged circular pipe. *Phys. Rev.* **73**, 383–406.

MANI, R. 1973 Refraction of acoustic duct waveguide modes by exhaust jets. *Q. Appl. Maths* **30**, 501–520.

MASSEY, K. C., AHUJA, K. K., JONES, R. R. III & TAM, C. K. W. 1994 Screech tones of supersonic heated free jets. *AIAA Paper* 93-0141.

MORGAN, J. D. 1974 The interaction of sound with a semi-infinite vortex sheet. *Q. J. Mech. Appl. Maths* **27**, 465–487.

MUNT, R. M. 1977 The interaction of sound with subsonic jet issuing from a semi-infinite cylindrical pipe. *J. Fluid Mech.* **83**, 609–640.

MUNT, R. M. 1990 Acoustic transmission properties of a jet pipe with subsonic jet flow: I. The cold jet reflection coefficient. *J. Sound Vib.* **142**, 413–436.

NOBLE, B. 1988 *Methods based on the Wiener-Hopf technique*, 2nd edn. Chelsea.

ORSZAG, S. A. & CROW, S. C. 1970 Instability of a vortex sheet leaving a semi-infinite plate. *Stud. Appl. Maths* **49**, 167–181.

PINKER, R. A. & BRYCE, W. D. 1976 The radiation of plane wave duct noise from a jet exhaust, statically and in flight. *AIAA Paper* 76-581.

RIDDERS, C. J. F. 1982 Accurate computation of $f'(x)$ and $f'(x)f''(x)$. *Adv. Engng Softw.* **4**, 75–76.

RIENSTRA, S. W. 1983 A small Strouhal number analysis for acoustic wave-jet flow-pipe interaction. *J. Sound Vib.* **86**, 539–556.

RIENSTRA, S. W. 1984 Acoustic radiation from a semi-infinite annular duct in a uniform subsonic mean flow. *J. Sound Vib.* **94**, 267–288.

RIENSTRA, S. W. 2007 Acoustic scattering at a hard–soft lining transition in a flow duct. *J. Engng Maths* **59**, 451–475.

SAMANTA, A. 2008 Finite-wavelength scattering of incident vorticity and acoustic waves at a shrouded-jet exit. PhD thesis, University of Illinois at Urbana-Champaign.

SAVKAR, S. D. 1975 Radiation of cylindrical duct acoustic modes with flow mismatch. *J. Sound Vib.* **42**, 363–386.

SEBOURN, C. L. & SHOPE, F. L. 2005 Research summary on the AEDC ASTF C-2 aeroacoustic resonance phenomenon. *AIAA Paper* 2005-2932.

STRANGE, P. J. R. & CRIGHTON, D. G. 1983 Spinning modes on axisymmetric jets. Part 1. *J. Fluid Mech.* **134**, 231–245.

SUZUKI, T. & COLONIUS, T. 2006 Instability waves in a subsonic round jet detected using a near-field phased microphone array. *J. Fluid Mech.* **565**, 197–226.

TAM, C. K. W., AHUJA, K. K. & JONES, R. R. III 1994 Screech tones from free and ducted supersonic jets. *AIAA J.* **32**, 917–922.

TAYLOR, M. V., CRIGHTON, D. G. & CARGILL, A. M. 1993 The low frequency aeroacoustics of buried nozzle systems. *J. Sound Vib.* **163**, 493–526.

VEITCH, B. & PEAKE, N. 2007 Models for acoustic propagation through turbofan exhaust flows. *AIAA Paper* 2007-3543.

VEITCH, B. & PEAKE, N. 2008 Acoustic propagation and scattering in the exhaust flow from coaxial cylinders. *J. Fluid Mech.* (in press).